

NASA Contractor Report 181924, Volume I

(NASA-CR-181924-Vol-1) DEVELOPING AND
UTILIZING AN EULER COMPUTATIONAL METHOD FOR
PREDICTING THE AIRFRAME/PROPULSION EFFECTS
FOR AN AFT-MOUNTED TURBOPROP TRANSPORT.
VOLUME 1: THEORY DOCUMENT Final(Boeing

N91-24118

Unclas

63/02 0019374

Developing and Utilizing an Euler Computational Method for Predicting the Airframe/Propulsion Effects for an Aft-Mounted Turboprop Transport

Volume I: Theory Document

H. C. Chen and N. Y. Yu

**Boeing Commercial Airplane Group
Seattle, Washington**

**Contract NAS1-18703
March 1991**



National Aeronautics and
Space Administration

Langley Research Center
Hampton, Virginia 23665-5225

1. Table of Contents

1. Summary	1
2. Introduction	1
3. Global Flowfield Solution	2
a. Grid Generation	2
b. Euler Flow Solver	3
c. Numerical Validation	5
4. Embedded Flow Solution	7
a. Embedded-Region Grid Generation	7
b. Interpolation Method	8
c. Embedded Method	8
5. Results and Discussions	9
a. Global Flowfield Solution	9
b. Embedded Flow Solution	10
6. Conclusion	10
7. Acknowledgement	11
8. References	12
9. Appendices	14
A. Grid Generation Equations	15
B. Numerical Method for the Euler Solver	17
C. Boundary Condition Implementations	20
D. Interpolation Method	24

1. Summary

An Euler flow solver has been developed for predicting the airframe/propulsion integration effects for an aft-mounted turboprop transport. This solver employs a highly efficient multigrid scheme, with a successive mesh-refinement procedure to accelerate the convergence of the solution. A new dissipation model has also been implemented to render solutions that are grid insensitive. The propeller power effects are simulated by the actuator disk concept. An embedded flow-solution method has been developed for predicting the detailed flow characteristics in the local vicinity of an aft-mounted propfan engine in the presence of a flowfield induced by a complete aircraft. Results from test case analysis are presented. A user's guide for execution of computer programs, including format of various input files, sample job decks, and sample input files, is provided in an accompanying volume.

2. Introduction

There is a strong need for computational aerodynamics codes for the analysis of complete aircraft configurations. A method for airframe/engine integration must correctly include all the complexity of the flow. Computational methods can provide detailed knowledge of the flow and aid in the design of superior configurations in a cost-effective manner. In recent years, significant progress has been made in the development of numerical methods for general three-dimensional analysis. However, much research work remains to be done in the area of transonic, rotational flow analysis for complex airplane configurations with multiple lifting surfaces. The rotational flow analysis is necessary for analyzing a turboprop transport because of the swirl behind the propeller plane.

The objective of the present study is to develop a new computer program that can simulate the complex flowfield produced by an advanced aft-mounted propfan aircraft. This includes the development of an embedded flow solution method for predicting the detailed flow characteristics in the local vicinity of an aft-mounted

propfan engine in the presence of a flowfield induced by a complete aircraft.

This program can be used to predict/evaluate the airframe/engine integration effects of a complete wing/body/tail/aft-mounted propfan configuration, as well as the effects of engine power on lateral stability (Ref. 1). This program can also be used as a technology basis for the development of an aerodynamic design capability for aft-mounted propfan aircraft by coupling the program with an automated iteration procedure developed at Langley (Ref. 2).

3. Global Flowfield Solution

A solution method that can predict the global flowfield about a complete aircraft configuration with aft-mounted engines has been developed. The global flowfield solution method includes two major steps. These are: a. the generation of the computational grid, and b. the development of Euler flow solver. The numerical validation of the global solution method is also discussed to show how the method works.

a. Grid Generation

The analysis of a complete airplane, such as that shown in Fig. 1, requires the use of a grid system that will yield accurate solutions at affordable cost using existing supercomputers. The unstructured-grid approach (Refs. 3, 4) offers great flexibility in treating complex geometry. However, the unstructured-grid flow solver requires a large central memory, and the solution algorithm is less efficient and less accurate than the structured-grid counterpart on a comparable grid. The rectangular-grid approach (Ref. 5) is an alternative, provided automatic mesh refinement can be done effectively and accurately. The present work utilizes a structured surface-fitted grid. In this approach, the grid on the configuration surface is generated first, and then the flowfield grids are obtained using an elliptic grid generation scheme. This offer two major advantages: firstly, the structured-grid requires minimum storage for the flow solution algorithm since the grid points are well ordered, and secondly, the surface-fitted grid allows for easier and more accurate implementation of the boundary conditions compared to a non-surface-

fitted grid.

To generate grids for a complex aircraft configuration, a block-structured grid is used. The complete flowfield is divided into a number of convenient blocks so that smooth 3D grids can be generated in each block. Fig. 2 illustrates the present blocking strategy. A surface passing through the middle of the nacelle together with a surface passing through the T-tail plane (shown in dashed lines) is used to divide the complete flowfield into four blocks. Within each block, a 3D elliptic grid generation technique is derived from the method of Thompson (Refs. 6, 7). Source terms based on boundary grid distributions are added to the grid generation equations to control grid spacing and grid orthogonality in the flowfield. Details on grid generation equations and the implementation of source terms are discussed in Appendix A.

The grid topology used in the present work is a C-type grid about the wing, an H-type grid about the strut, and the T-tail as illustrated in Fig. 3. The grid in the spanwise direction is of the H type. The crown and keel lines of the fuselage form one of the C lines. The leading edge and trailing edge of vertical tail are fitted with grid lines. The grid on the nacelle surface and plume that extends downstream to the far field is H type. To illustrate the grid topology used in the present analysis, the field grid on spanwise, streamwise and normal direction cuts are shown in Figs. 4, 5 and 6 respectively. Fig. 7 shows a complete surface grid and part of the field grids for an aft-mounted propfan airplane.

b. Euler Flow Solver

The present Euler analysis method is based on a cell-centered, finite-volume, out-of-core multigrid Euler solver for a complete aircraft analysis (Ref. 1). The outermost iterative procedure carries out the successive mesh refinement. Starting from the coarsest mesh level, the entire flowfield is divided into blocks and the entire flowfield data is stored on a solid state disk (SSD). The computation is done in a block-by-block manner through the use of highly efficient input/output data management. The flowfield in each block is advanced in time through one multigrid cycle (Ref. 8). Within each multigrid level, a five-stage, explicit, Runge-Kutta time integration scheme, together with an implicit residual smoothing

method, is used to update the flow variables to a new time level. The updated flowfield data are then moved to the SSD before another block of flowfield data is transferred to the central memory. The block boundary data, needed for the adjacent blocks in flux and dissipation term calculations, are saved in different location on SSD, so that they can easily be fetched during the calculation process.

At the present time, the program is written in such a way that the flowfield can be divided in an arbitrary number of blocks in both normal and spanwise directions to handle large problems. However, the general strategy is to keep the number of blocks to a minimum, such that the program can be executed efficiently in a vector machine. Optimum blocking strategy can be different to fit a specific machine architecture. For a machine with very large directly addressable memory (e. g., CRAY-2 with 128 MW of memory), the entire flowfield may be divided into one to three blocks depending on the geometry complexity of the configuration. The converged solution at a given mesh level for the entire flowfield is interpolated to the next finer mesh level to start the Euler calculation on that mesh. Successive mesh refinement stops when the solution has converged at the finest mesh level. The basic numerical scheme used is discussed in Appendix B.

In the calculation process, the type of boundary condition along each boundary surface of a given block is specified. If it is an interblock boundary surface, conservation of mass, momentum, and energy are ensured with the adjacent block. Also, the flux term due to dissipation must be formulated precisely to satisfy the conservation laws across the block boundary. Due to the use of fourth-order dissipation terms, two layers of data from every adjacent block are needed in order to formulate a flux term that is identical to the one used in single-block calculations. For a far-field boundary surface, characteristic boundary conditions that take proper account of inflow and outflow conditions are implemented. Along a solid boundary surface, the conventional normal momentum equation is used to compute the surface pressure. The propeller power loading is simulated by an actuator disk where the total pressure, total temperature, and swirl distributions are prescribed (Ref. 1).

Another way of simulating propeller power effects is to prescribe the thrust, normal force, and side force along the propeller disk and the work added to the

flow by the propeller. The flow variables downstream of the disk are related to their upstream values through the use of continuity, momentum, and energy equations. The major advantage of this method is that the effects of angle of attack, as well as the influence of side flow, can easily be simulated through the input of normal force and side force distributions along the propeller disk. A detailed formulation of this method can be found in Reference 9. Boundary condition methods for engine inlet and exhaust are given in Reference 10. For the global analysis of an aft-mounted propfan transport, some simplification has been made. The primary exhaust flow of the engine is treated as a solid body with the shape obtained from an isolated nacelle or propfan analysis. The flowfield inside the plume is not computed, but this is a small region compared with the propeller slipstream. Boundary condition implementations are reviewed in Appendix C.

Important improvements have been made to the dissipation formulation to provide more accurate and reliable solutions for complex geometry. The spectral radius scaling of dissipation terms (Refs. 11, 12) has been adapted to the Euler code. The new formulation improves the consistency of the solution by decreasing sensitivity to the dissipation parameters and to the quality of the grid. This improvement over conventional dissipation formulations (Ref. 13) is especially pronounced on grids with a large aspect ratio or with nonsmooth mesh distributions (Ref. 14).

The focus of this study is in the subsonic and transonic speed region. However, the analysis method developed under present study also works for supersonic flow and is directly applicable to High Speed Civil Transport (HSCT) type of configurations. Numerical validation of the method in the transonic region is given in the next subsection.

c. Numerical Validation

Employment of both successive mesh refinement and the multigrid acceleration scheme is effective in speeding up the convergence of the solutions to steady state. For a typical flow solution of a wing-body-winglet configuration containing 200,000 grid points, three levels of mesh refinement are used in the calculations. On the first two mesh levels, 200 multigrid cycles are used. The fine mesh results

for a wing-body-winglet analysis at 25 and 50 multi-grid cycles are compared with the results at 200 cycles in Fig. 8. The differences in solutions are hardly discernable after 50 multigrid cycles on the fine mesh. To obtain a similarly converged solution without using successive mesh refinement requires more than 100 multigrid cycles in the fine mesh. For transonic cases with strong shocks, successive mesh refinement reduces the multigrid cycles from 400 to 200 on the fine mesh. The shock capturing scheme in the present Euler solver typically smears out the shock discontinuities over three to five grid points. The convergence of the shock discontinuities is more efficient when successive mesh refinement is used.

For the consistency test with respect to dissipation parameters, Euler analyses for a wing-body-winglet configuration with two different sets of dissipation parameters were conducted. In Fig. 9, symbols show a solution using dissipation parameters twice as large as those for the solution given by the solid line. The two results are very close, although increasing the values of the dissipation parameters appears to smooth out some of the local variations in the solution. Important flow features, such as the peaks and locations of the leading edge expansions, are unchanged from the wing-root to the tip of the winglet.

For the grid sensitivity test, the Euler solutions on two grids with significantly different grid quality were obtained for comparison. Both grids contain 200,000 points and have identical surface grid distributions. However, Grid-1 has a strong kink at the tip of the winglet, whereas Grid-2 is smooth near the tip of the winglet. The differences in solutions due to these grid effects are small and localized (Fig. 10). Away from the tip of the winglet, the differences are essentially non-discernable. Again, important flow features such as shock locations are unchanged throughout the entire wing.

A convergence study of the Euler solutions with respect to mesh refinement requires the use of an extremely fine mesh. This becomes prohibitively expensive in 3D. Therefore, a 2D version of the Euler code was employed for such studies. We chose the NLR7301 shockfree airfoil as a test case. Four successive levels of grids were used starting from grid-1 of 40x8, then grid-2 of 80x16, grid-3 of 160x32, and ending with grid-4 of 320x64 (Fig. 11). The Euler solution in grid-1

is noticeably different from the finer grid solutions. The airfoil geometry is not very well defined in this grid. As the grid is refined, it is seen that the solutions on grid-2 and -3 are reasonably close to the finest grid solution on grid-4. This suggests that the 160x32 grid is adequate for this type of calculation.

4. Embedded Flow Solution

A capability has been developed for the computation of the detailed flow characteristics in the local vicinity of an aft-mounted propfan engine in the presence of a flowfield induced by a complete aircraft configuration at subsonic and transonic speeds. The method used in the present study is to embed fine grids about the aft-mounted propfan engine and to solve the Euler equations on this grid using boundary conditions interpolated from a global Euler solution. Details on the local grid generation and the embedded procedure for the local flow field are discussed in the following subsections.

a. Embedded-Region Grid Generation

To resolve a detailed flow field in the propfan nacelle region, grids with suitable topology are generated. For a strut-mounted, domed nacelle with propeller disk, shown in Fig. 12, a cylindrical grid that wraps around the nose of the nacelle is used. In the case of a propfan nacelle with inlet and exhaust, a cylindrical C-type grid wrapped around the fan cowl leading edge, shown in Fig. 13, is used. In either case, an H-type grid is used along the strut. The external boundary is obtained by constructing circular cross section in the streamwise direction with a given radius R , where R is set equal to the distance between nacelle centerline and the strut/fuselage intersection. The upstream and downstream boundary can be set by the user through input. The number of grid points in each coordinate direction are also input by the user. A typical strut-mounted, domed nacelle shown in Fig.12 uses 101x21x25 grids with 81x25 points on the nacelle surface, 81x21 points on the strut, and 13x25 points on the propeller disk. The local grid is generated independently of the global configuration and the global grid system. The outer boundary surface of the local grid does not have to be one of the grid faces of the global system. Interpolations of the global flow variables onto the local grids are

needed in order to establish the boundary condition as well as the initial condition for the local embedded analysis.

b. Interpolation method

The global flowfield solution can be computed as described in Section 3. A dense local grid about the aft-mounted propfan engine can then be generated. Such a grid will allow resolution of such geometry details as the inlet lip and strut leading edge. The solution from the global flowfield analysis are extracted and used as boundary conditions for the embedded region through interpolation (Figs. 12, 14). More details about the interpolation method are given in Appendix D.

c. Embedded Method

An Euler solver based on the same technology used in the global solution method is developed to solve the detailed flow field around the aft-mounted propfan engine. The interpolated global flow solution is used as an initial condition for the embedded flowfield and the boundary condition in the far-field. As the solution evolves, the far-field boundary condition is updated according to characteristic relations derived from the local one-dimensional Euler equations shown in Appendix C. The implementation of a characteristic boundary condition is needed in order to prevent the disturbances reflecting back to the flowfield. Other types of boundary conditions are implemented to the solver in the same way as the global solution method and are described in Appendix C.

The present grid embedding approach assumes that the global flow solution provides adequate resolution in the region away from the local embedded region, such that the interpolated data can be used as boundary condition for the embedded region. No iterative procedure between the global solution and the embedded solution is used in the present work. A better approach of resolving flowfield details around a complex aircraft configuration is to use a general multiblock approach, where a high resolution multiblock grid can be generated and used for each individual block.

5. Results and Discussions

Results from global flowfield analysis will be presented first followed by the embedded solution. How to use the program for these analyses is described in Volume II (Ref. 15).

a. Global Flow Solution

An aft-mounted propfan configuration shown in Fig. 15 is analyzed to demonstrate the capability of the out-of-core Euler flow solver. The grid system consists of $241 \times 37 \times 33$ points with 81×25 points on the wing, 65×9 points on the strut, 37×17 points on the horizontal tail, 27×13 points on the vertical tail, 24×69 points on nacelle and plume, and 2925 points on the fuselage.

The flow conditions are set at $M_\infty = 0.8$, $\alpha = 1.5$ deg. The propeller power conditions are thrust coefficient = 0.1232, zero normal force and side force coefficients. The isobars for the complete aircraft are shown in Fig. 16. Figures 17 through 19 show the detailed Mach contours in the aftbody regions for propeller-on and propeller-off cases. It can be seen that the flow accelerates substantially in the aftbody regions for the propeller power-on case. Fig. 19 reveals the formation of a supersonic zone on the lower surface near the nacelle-strut junction. This occurs for both propeller power-on and power-off cases. The analysis identifies potential aerodynamic problems of the configuration such as wave drag penalty.

The analysis information provides opportunities for engineers to recontour or redesign the problem areas of the aircraft. The present analysis capability can therefore complement the wind tunnel test to render a superior aerodynamic design in the aircraft development process. The effectiveness of the analysis capability developed in the present study can be further improved by coupling our capability with an automated iterative procedure for aerodynamic design developed at NASA Langley (Ref. 2).

A crucial issue for aft-mounted propfan engine installations is the wing wake location relative to propeller blade location. Specifically, the intersection of wing

wake with propeller blade should be avoided. The streamline tracing capability developed in the present study can serve this function very well. The streamlines emitted from the trailing edge of the wing for the previously analyzed case are shown in Fig. 20.

b. Embedded Flow Solution

A strut-mounted domed, nacelle shown in Fig. 12 is analyzed to demonstrate the embedded Euler solution. The far-field boundary condition is provided by the global flowfield solution through interpolation, and the propeller power conditions are the same as that in the global solution. Figures 21 and 22 show the Mach number contours of the embedded nacelle-strut from the embedded Euler solution. This trend is similar to the results from the global solution; however, considerably more detail can be seen in the embedded solution (Fig. 23) due to the use of a high resolution local embedded grid.

The grid embedding can provide a very useful capability for predicting the detail flow characteristics in the local vicinity of an aft-mounted propfan engine in the presence of a flowfield induced by a complete aircraft. However, the procedure for embedded flow solution (described in Section 4) involves several steps and would require that the global solution be carried out first. Furthermore, the current grid embedding procedure does not allow the local embedded solution to feed back to the global flowfield. To fully couple the global and local flowfield would require additional iteration. A better approach of resolving flowfield details around a complex aircraft configuration is to use a general multiblock approach, where high resolution multiblock grid can be generated and used for each individual block.

6. Conclusion

A highly efficient and accurate Euler solver for predicting the airframe/propulsion integration effects for an aft-mounted turboprop transport aircraft configuration has been developed. The solution method is insensitive to grid quality and dissipation parameters. Convergence of the solution with respect to mesh refinement was demonstrated in 2D to further assess the numerical

accuracy of the Euler solutions. An embedded flow solution capability has been developed for predicting the detailed flow characteristics in the local vicinity of an aft-mounted propfan engine in the presence of a flowfield induced by a complete aircraft.

7. Acknowledgement

The Authors wish to thank Kazu Kusunose of The Boeing Company for his contribution in the development of the grid generation program for the global flow analysis.

8. References

1. Yu, N. J., Kusunose, K., Chen, H. C. and Sommerfield D. M., "Flow Simulations for a Complex Airplane Configuration Using Euler Equations," AIAA Paper 87-0454, Jan. 1987.
2. Campbell R. L. and Smith L. A., "A Hybrid Algorithm for Transonic Airfoil and Wing Design," AIAA Paper 87-2552-CP, 1987.
3. Jameson, A. and Baker, T. J., "Improvement to the Aircraft Euler Method," AIAA Paper 84-0093, 1984.
4. Peraire, J., Peiro, J., Formaggia, L., and Morgan, K., "Adaptive Numerical Solutions of the Euler Equations in 3D Using Finite Elements," 11th ICNMF, Lecture Notes in Physics, Vol. 323, Springer-Verlag, 1989.
5. Samant, S. S., Bussoletti, J. E., Johnson, F. T., Melvin, R. G., and Young, D. P., "Transonic Analysis of Arbitrary Configurations Using Locally Refined Grids," 11th ICNMF, Lecture Notes in Physics, Vol. 323, Springer-Verlag, 1989.
6. Kusunose, K., D. L. Marcum, Chen, H. C. and N. J. Yu, "Transonic Analysis of Complex Airplane Configurations," AIAA Paper 87-1196, June 1987.
7. Thompson, J. F., Editor, "Numerical Grid Generation," North Holland, 1982.
8. Jameson, A. and Baker, T. J., "Multigrid Solution of the Euler Equations for Aircraft Configurations," AIAA Paper 84-0093, 1984.
9. Yu, N. J., Chen, H. C., Chen, "Flow Simulations for Nacelle-Propeller Configurations Using Euler Equations," AIAA Paper 84-2143, 1984.
10. Chen, H. C., Yu, N. J. Rubbert, P. E., and Jameson A., "Flow Simulations for General Nacelle Configurations Using Euler Equations," AIAA 83-0539, 1983.
11. Jameson, A., "Successes and Challenges in Computational Aerodynamics," AIAA Paper 87-1184, 1987.
12. Swanson, R. C. and Turkel, E., "Artificial Dissipation and Central Difference

- Schemes for the Euler and Navier-Stokes Equations," AIAA Paper 87-1107, 1987.
13. Jameson, A., Schmidt, W., and Turkel, E., "Numerical Solutions of the Euler Equations by Finite Volume Methods Using Runge-Kutta Time-Stepping Scheme," AIAA 81-1259, 1981.
 14. Chen, H. C., Yu, N. J., "Development of a Highly Efficient and Accurate 3D Euler Flow Solver," 11th ICNMF, Lecture Notes in Physics, Vol. 323, Springer-Verlag, 1989.
 15. Chen, H. C., H. E. Nebeck, Kao, T. J., Yu, N. J., and Kusunose, K., "Developing and Utilizing an Euler Computational Method for Predicting the Airfram/Propulsion Effects for an Aft-Mounted Turboprop Transport, Volume II: User Guide," NASA CR-181924, March 1991.

9. Appendices

Appendix A

Grid Generation Equations

A grid generation method based on the solution of a set of elliptic grid generation equations

$$\xi_{xx} + \xi_{yy} + \xi_{zz} = P \quad (A1)$$

$$\eta_{xx} + \eta_{yy} + \eta_{zz} = Q \quad (A2)$$

$$\zeta_{xx} + \zeta_{yy} + \zeta_{zz} = R \quad (A3)$$

are used in the present work. Here x, y, z are physical coordinates and ξ, η, ζ are the computational coordinates. P, Q , and R are the added source terms to control the grid spacing in the flow field. The strength of the source terms is dictated by the boundary grid distributions and is written in terms of the first and second derivatives of the arc length distributions along the boundary surfaces by

$$P = -(S_i)_{\xi\xi} / (S_i)_{\xi} \quad (A4)$$

$$Q = -(S_j)_{\eta\eta} / (S_j)_{\eta} \quad (A5)$$

$$R = -(S_k)_{\zeta\zeta} / (S_k)_{\zeta} \quad (A6)$$

where S_i, S_j, S_k represent arc length of a grid line along the boundary surface. These source terms are computed along each boundary surface and are interpolated into the flow field using a simple linear interpolation method. Because the source strength varies smoothly from one boundary surface to another, the interior grid

distribution will also vary smoothly from one surface to another surface. Additional weighting functions can be introduced to further increase the controllability of the field grids.

Appendix B

Numerical Method for the Euler Solver

The basic numerical scheme follows Jameson's finite volume formulation of solving the Euler equations

$$\partial w / \partial t + \partial f / \partial x + \partial g / \partial y + \partial h / \partial z = 0 \quad (B1)$$

$$w = \begin{bmatrix} \rho \\ \rho u \\ \rho v \\ \rho w \\ \rho E \end{bmatrix} \quad f = \begin{bmatrix} \rho u \\ P + \rho u^2 \\ \rho uv \\ \rho uw \\ \rho uH \end{bmatrix} \quad g = \begin{bmatrix} \rho v \\ \rho vu \\ P + \rho v^2 \\ \rho vw \\ \rho vH \end{bmatrix} \quad h = \begin{bmatrix} \rho w \\ \rho wu \\ \rho wv \\ P + \rho w^2 \\ \rho wH \end{bmatrix}$$

Here, the conventional notations ρ , u , v , w , P , E are used for density, three components of velocity, pressure, and the total energy. The total enthalpy H is defined as

$$H = E + P/\rho = \gamma P/(\gamma - 1)\rho + (u^2 + v^2 + w^2)/2 \quad (B2)$$

with γ representing the ratio of specific heat. In the governing equations, the density and the pressure are normalized with respect to its freestream values. The

total energy and the total enthalpy are normalized with respect to P_∞/ρ_∞ , and the velocity is normalized with respect to the square root of P_∞/ρ_∞ .

The unsteady Euler equations are solved by the multistage Runge-Kutta time-stepping scheme

$$\begin{aligned}
w^{(0)} &= w^n \\
w^{(1)} &= w^{(0)} - \alpha_1 \Delta t R^{(0)} \\
&\dots\dots\dots \\
w^{(m-1)} &= w^{(0)} - \alpha_{m-1} \Delta t R^{(m-2)} \\
w^{n+1} &= w^{(m)} = w^{(0)} - \Delta t R^{(m-1)}
\end{aligned}
\tag{B3}$$

Here, $C(w)^{(m)}$ represents convective flux terms, and $D(w)^{(m)}$ represents artificial dissipation terms added to control numerical oscillations. Central difference approximations are used for both convective and dissipative term calculations. A spectral radius scaling on the dissipation terms is used to minimize the amount of artificial dissipations, as shown in the following

$$D(w)_i = d_{i+1/2,j,k} - d_{i-1/2,j,k} \quad (B4)$$

$$d_{i+1/2,j,k} = \lambda_{i+1/2,j,k}(\epsilon^{(2)} - \epsilon^{(4)}\delta_\xi^2)(W_{i+1,j,k} - W_{i,j,k}) \quad (B5)$$

where $\lambda_{i+1/2,j,k}$ is the spectral radius at face $i+1/2$, and is defined as

$$\lambda_{i+1/2,j,k} = (q_{n_{i+1/2,j,k}} + a_{i+1/2,j,k})S_{i+1/2,j,k} \quad (\text{B6})$$

Within each block of the flow field, a V-cycle multigrid scheme is used provided the number of cells in each coordinate direction can be divided by 2 to the n th power, with $n+1$ representing the number of multigrid levels.

Appendix C

Boundary Condition Implementations

The boundary conditions encountered in the complete airplane analysis include: 1) Solid-surface boundary condition, 2) Far-field boundary condition, 3) Nacelle-inlet boundary condition, and 4) nacelle exhaust plane/propeller disk boundary conditions. Each type of boundary condition implementation is described in the following subsections:

1). Solid-surface boundary condition

Along the configuration surface, the tangency condition is enforced by setting $\bar{q} \cdot \bar{n} = 0$. For the cell-centered scheme used in the present work, the pressure on the configuration is also needed to evaluate the convective flux terms in the momentum and energy equations. Simple extrapolation from the flowfield solution can be used. However, to improve numerical accuracy, a normal momentum equation that relates the normal derivative of pressure to the streamwise and spanwise derivatives is used, i. e., along surface $l=2$, one has

$$S_{2j}S_{ij} \partial P / \partial \xi_i - \rho U_i U_j \partial (S_{2j}) / \partial \xi_i = 0 \quad (C1)$$

$$\text{with } S_{ij} = h \partial \xi_i / \partial x_j, \text{ and } U_i = S_{ij} u_j, \quad h = |\partial x_i / \partial \xi_j|$$

2). Far-field boundary condition

Because the calculation is performed in finite region, correct implementation of far-field boundary condition is essential for numerical accuracy as well as for numerical stability. In the present study, the characteristic boundary condition based on locally one-dimensional Euler equations is used. Along each face of the far-field boundary cell, the normal velocity is computed and checked. For

subsonic freestream condition, if it is an inflow boundary, one Riemann variable extracted from the interior flow field together with the tangential velocity, the enthalpy, the entropy and another Riemann variable evaluated from upstream values are used to determine all flow variables, i.e.,

$$\begin{aligned} q_t &= q_{t_\infty}, \quad S = S_\infty, \quad H = H_\infty, \\ q_n + 2a/(\gamma - 1) &= q_{n_e} + 2a_e/(\gamma - 1), \\ q_n - 2a/(\gamma - 1) &= q_{n_\infty} - 2a_\infty/(\gamma - 1). \end{aligned} \tag{C2}$$

For the subsonic outflow boundary, one Riemann variable based on freestream values together with four extrapolated quantities are used to calculate the flow variables, i.e.,

$$\begin{aligned} q_t &= q_{t_e}, \quad S = S_e, \quad H = H_e, \\ q_n + 2a/(\gamma - 1) &= q_{n_\infty} + 2a_\infty/(\gamma - 1), \\ q_n - 2a/(\gamma - 1) &= q_{n_e} - 2a_e/(\gamma - 1). \end{aligned} \tag{C3}$$

with subscript e representing values extrapolated from the interior flowfield. In the case of supersonic inflow boundary, all variables are assigned to their freestream values. For supersonic outflow boundary, all flow variables are extrapolated from the interior flow solutions.

3). Nacelle-inlet boundary conditions

Along the nacelle inlet face, it is treated as an outflow boundary. Three choices of boundary conditions can be used:

a). Mass flux boundary condition

If the capture stream tube area of the nacelle, i.e., A_∞ is given, the mass flux at the inlet face is given by

$$(\rho q_n)_f = (\rho_\infty A_\infty q_\infty)/A_f \quad (C4)$$

with A_f representing inlet face area.

b). Velocity boundary condition

For a given captured stream tube area A_∞ , one can convert the mass flux boundary condition into the velocity boundary condition using the isentropic relation to relate density to the local velocity, i.e.,

$$q_n/q_\infty = (A_\infty/A_f)[1 - (\gamma - 1)(M_\infty)^2 \{(q/q_\infty)^2 - 1\}/2]^{-1/(\gamma - 1)} \quad (C5)$$

A simple Newton's iteration procedure is written to solve the above nonlinear equation for q_n .

c). Pressure boundary condition

The static pressure P along the inlet face can be prescribed. The rest of the flow variables are extrapolated from the upstream flow field.

4). Nacelle exhaust plane/propeller disk boundary conditions

Along the nacelle exhaust plane, as well as along the downstream side of the propeller disk, similar boundary conditions can be applied. In either case, it is assumed to be a subsonic inflow boundary. The first type of boundary condition that can be applied to both nacelle and propeller disk prescribes the total pressure,

total temperature together with the swirl along the boundary. These quantities are then used to evaluate the flow variables according to the following formula

$$\begin{aligned}
 M^2 &= 5q^2 / \{7(T_t)^2 - q^2\} , \\
 p &= P_t / (1 + 0.2M^2)^{3.5} , \\
 \rho &= \gamma P / \{(\gamma - 1)(C_p T_t - q^2/2)\}
 \end{aligned}
 \tag{C6}$$

with q obtained from extrapolation. Another type of boundary condition frequently used for propeller simulation prescribes the thrust per unit area F_x , the normal force per unit area F_y , the side force per unit area F_z , and the power done by the propeller Q to calculate the flow variables downstream of the propeller disk, i.e.,

$$\begin{aligned}
 \rho U u + S_x P &= \rho_1 U_1 u_1 + S_x P_1 + S F_x , \\
 \rho U v + S_y P &= \rho_1 U_1 v_1 + S_y P_1 + S F_y , \\
 \rho U w + S_z P &= \rho_1 U_1 w_1 + S_z P_1 + S F_z , \\
 u^2 + v^2 + w^2 &= q^2 , \\
 \rho &= 3.5P / \{C_p T_{t1} + SQ/\rho U - q^2/2\}
 \end{aligned}
 \tag{C7}$$

with subscript 1 denoting upstream conditions and S_x (or S_y , S_z) is the projection area in x- (or y-, z-) direction of a cell face on the propeller disk, and S is the cell face area. In either type of propeller disk boundary condition method, the boundary condition along the upstream side of the propeller disk is obtained by setting the mass flux to be equal to the mass flux of the downstream side.

Appendix D

Interpolation Method

For the aft-mounted turboprop transport, the test case consists of 241x37x33 grid points (240x36x32 cells), the flowfield is divided into 3x2 blocks. There are three blocks in the J (normal) direction and two blocks in the K (spanwise) direction. There is no blocking in the I (wrap-around) direction. The cell dimension of each block is 240x12x16.

A reduced flowfield is obtained by using data from the inner two blocks in J direction. In addition, flow variables are calculated at the grid points through averaging. The reduced grid (and flowfield solution) consisting of 239x24x33 grid points is written in single block. The reduced flowfield will be used for interpolating the data onto the local embedded grid.

The local embedded grid consists of 101x21x25 grid points (100x20x24 cells). The cell center locations are computed for all cells as interpolation points for the interpolation of flowfield data from the reduced global solution. A cell-centered local embedded grid is then written in single block.

Within a cell in the reduced global flowfield, a flow variable can be interpolated using trilinear basis functions for any interpolation point within the cell, including the cell boundary. Let F be a variable (F may be a flow variable or one of the three physical coordinates), then within a cell

$$F = \sum_{m=1}^8 F_m N_m \quad (D1)$$

where

$$F_1 = F_{i,j,k}$$

$$F_2 = F_{i+1,j,k}$$

$$F_3 = F_{i,j+1,k}$$

$$F_4 = F_{i+1,j+1,k}$$

$$F_5 = F_{i,j,k+1}$$

$$F_6 = F_{i+1,j,k+1}$$

$$F_7 = F_{i,j+1,k+1}$$

$$F_8 = F_{i+1,j+1,k+1}$$

and N_m 's are the trilinear local basis functions defined as:

$$N_1 = (1 - \xi) (1 - \eta) (1 - \zeta)$$

$$N_2 = \xi (1 - \eta) (1 - \zeta)$$

$$N_3 = (1 - \xi) \eta (1 - \zeta)$$

$$N_4 = \xi \eta (1 - \zeta)$$

$$N_5 = (1 - \xi) (1 - \eta) \zeta$$

$$N_6 = \xi (1 - \eta) \zeta$$

$$N_7 = (1 - \xi) \eta \zeta$$

$$N_8 = \xi \eta \zeta$$

The ξ , η and ζ are the local coordinates bounded from 0 to 1

$$\xi = 0 \text{ at } i \text{ and } \xi = 1 \text{ at } i+1$$

$$\eta = 0 \text{ at } j \text{ and } \eta = 1 \text{ at } j+1$$

$$\zeta = 0 \text{ at } k \text{ and } \zeta = 1 \text{ at } k+1$$

Let a point P with physical coordinates (x, y, z) be in the cell for interpolation. We set $F = x$ (or y, z) in Eq. (D1) to obtain

$$\begin{bmatrix} x \\ y \\ z \end{bmatrix} = \sum_{m=1}^8 N_m \begin{bmatrix} x_m \\ y_m \\ z_m \end{bmatrix} \quad (D2)$$

We then solve Eq. (D2) for the local coordinates ξ , η , and ζ through Newton iteration starting from cell center values,

$$\xi = 0.5$$

$$\eta = 0.5$$

$$\zeta = 0.5$$

The computed local coordinates ξ , η , and ζ can then be used for interpolating a flow variable (e. g. pressure p) at the point P by setting $F = p$ in Eq. (D1).

Given an interpolation point P(x, y, z) in the local embedded grid, we need to find the cell in the (reduced) global flowfield that contains this point. Let a cell in the global flowfield be referenced by its lowest i, j, k indexes. For example, the cell in the previous discussion will be referenced by i, j, k. We may begin the search procedure at the cell corresponding to i=1, j=1, and k=1. We can then use Eq. (D2) to compute the local coordinates ξ , η and ζ . When any of the local coordinates is out of bound, the point P is considered not in the current cell. The values of the local coordinates will be used for stencil walk.

If $\xi < 0$ then move to a cell at $i-1$

If $\xi > 1$ then move to a cell at $i+1$

If $\eta < 0$ then move to a cell at $j-1$

If $\eta > 1$ then move to a cell at $j+1$

If $\zeta < 0$ then move to a cell at $k-1$

If $\zeta > 1$ then move to a cell at $k+1$

Increment (or decrement) of the indexes will not take place if the resulting cell is not within the reduced global flowfield.

Fig. 1. An Advanced Propfan Airplane Configuration

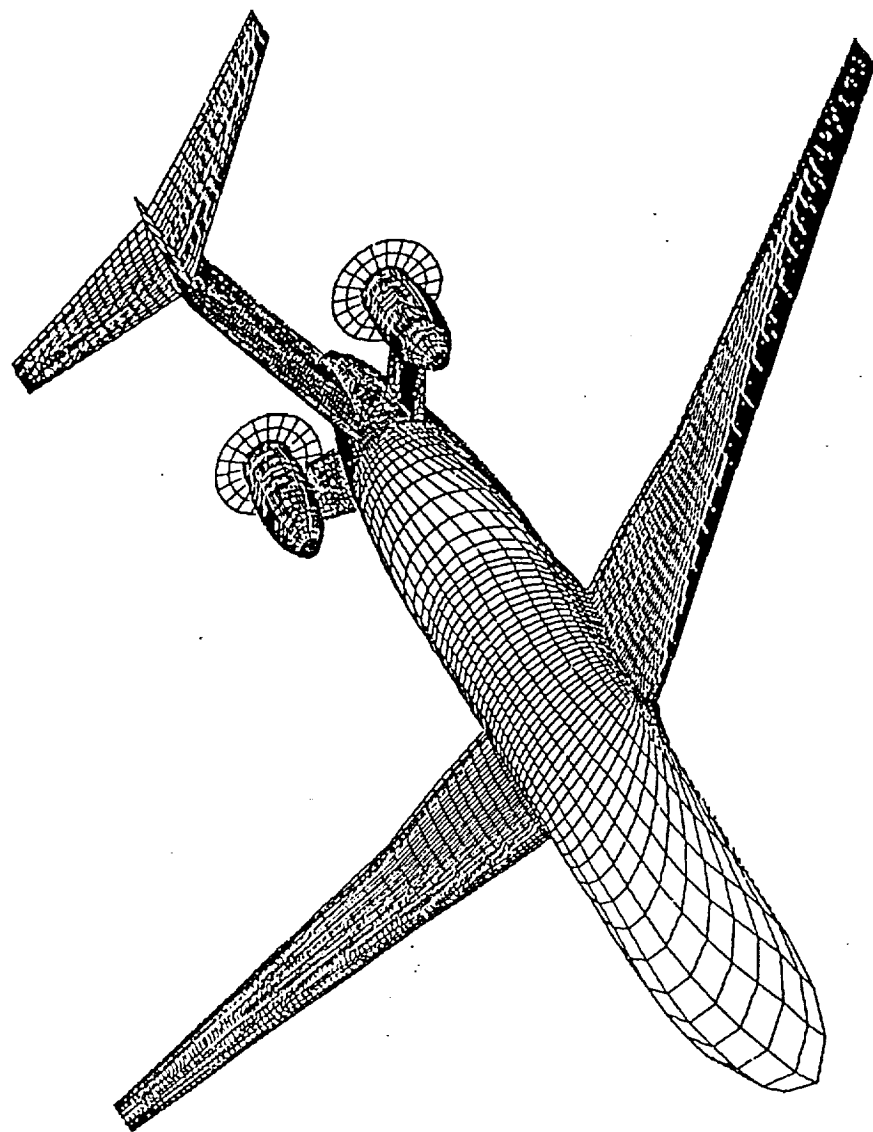


Fig. 2. Grid Generation and Blocking Strategy

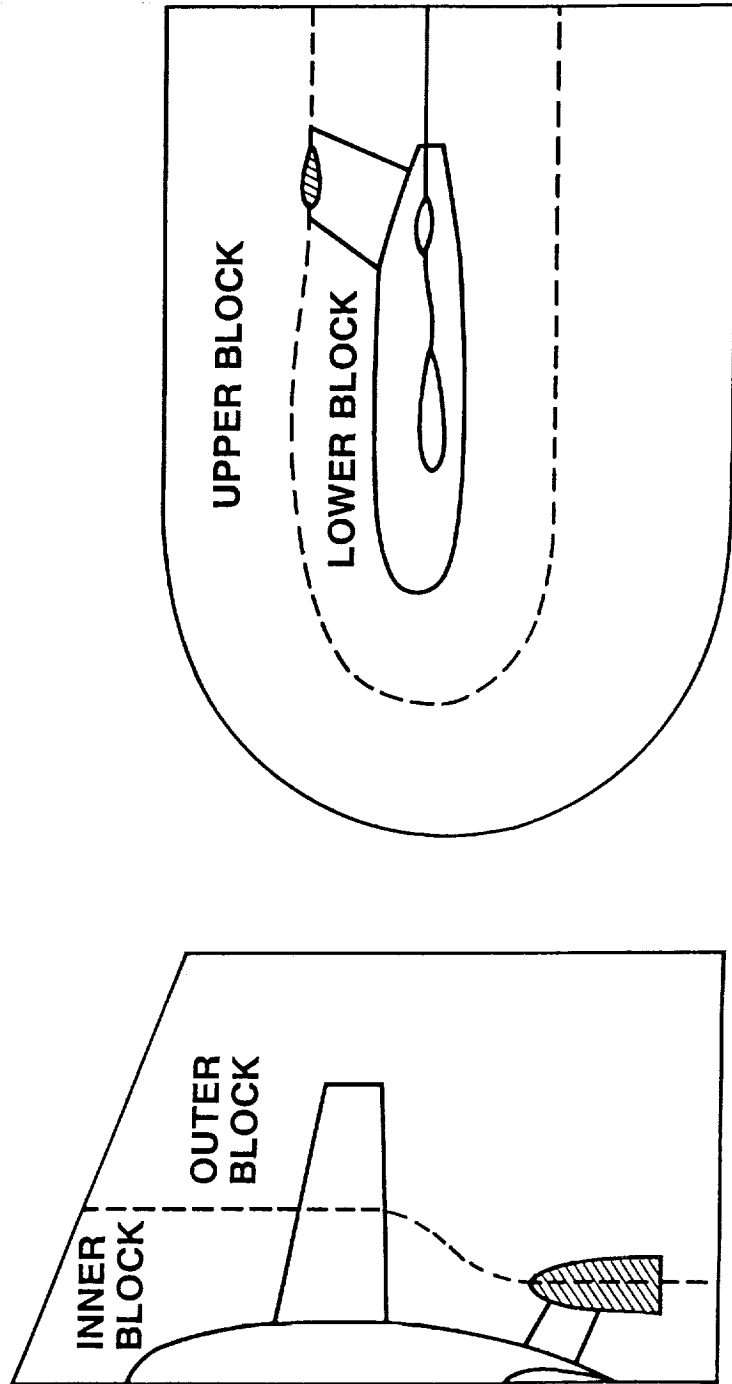


Fig. 3. Grid Topology at a Given Span Station

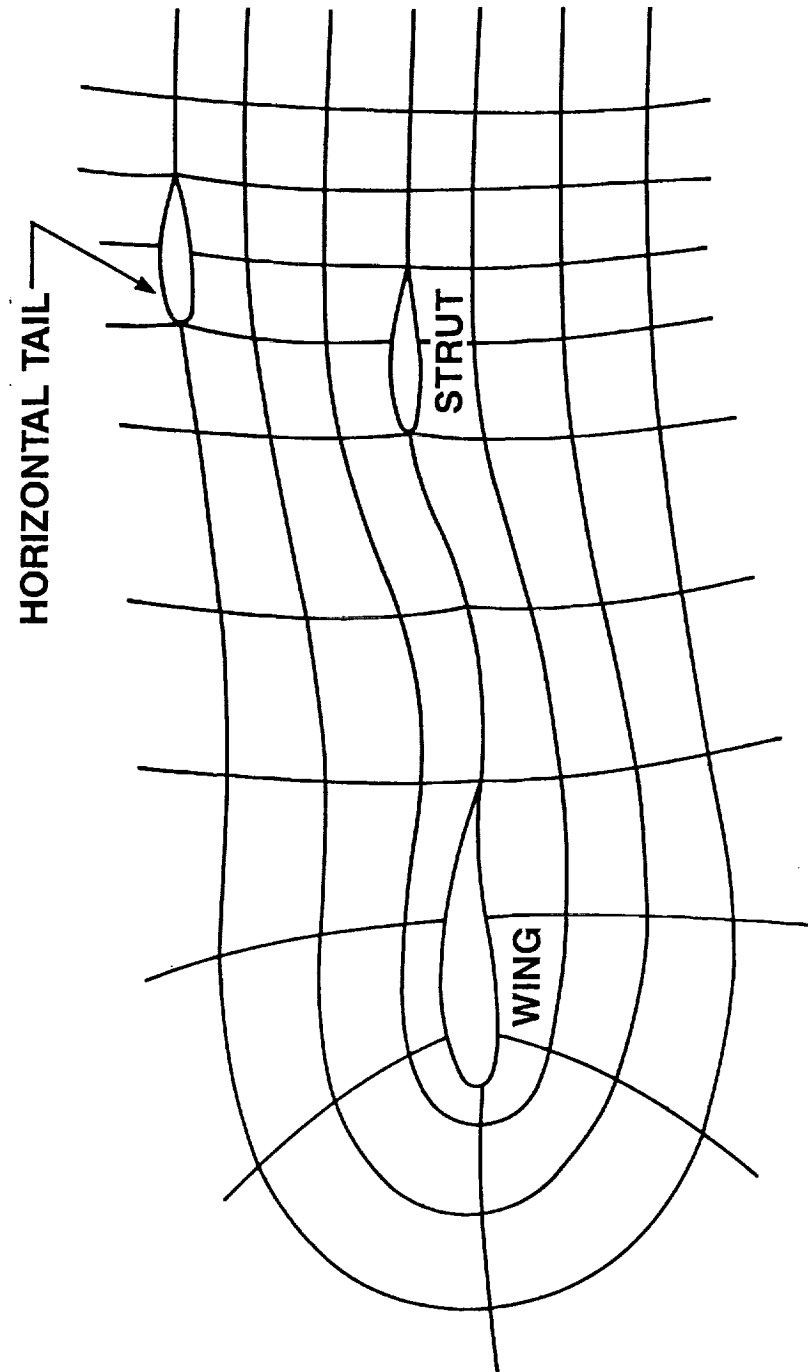
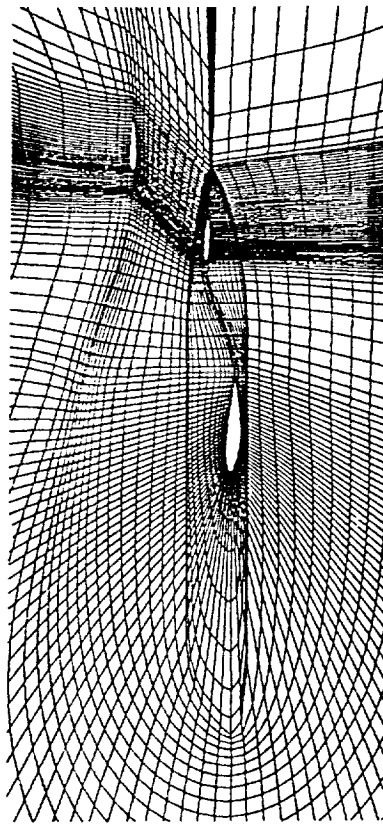
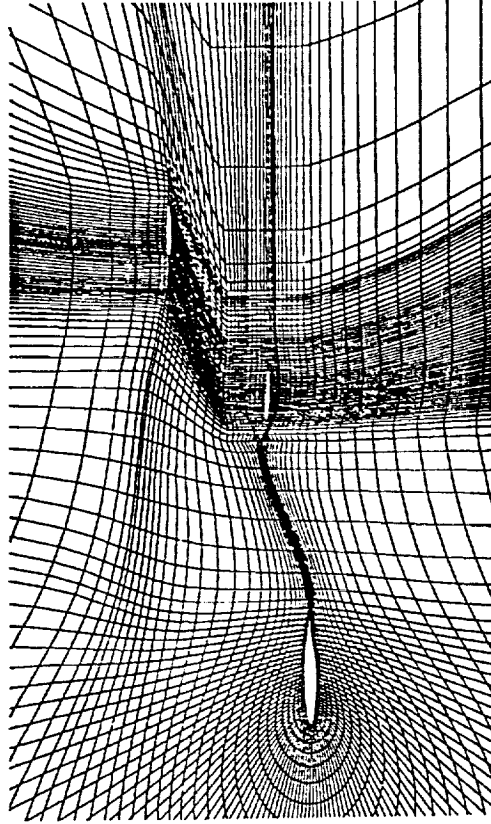


Fig. 4. Field Grids on Spanwise Cuts

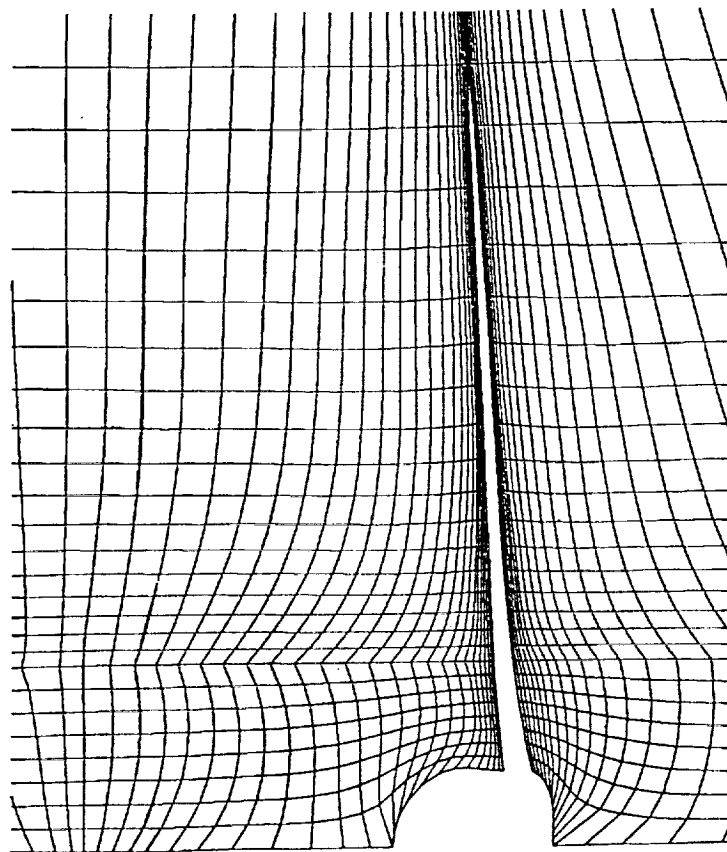


SIDE OF BODY

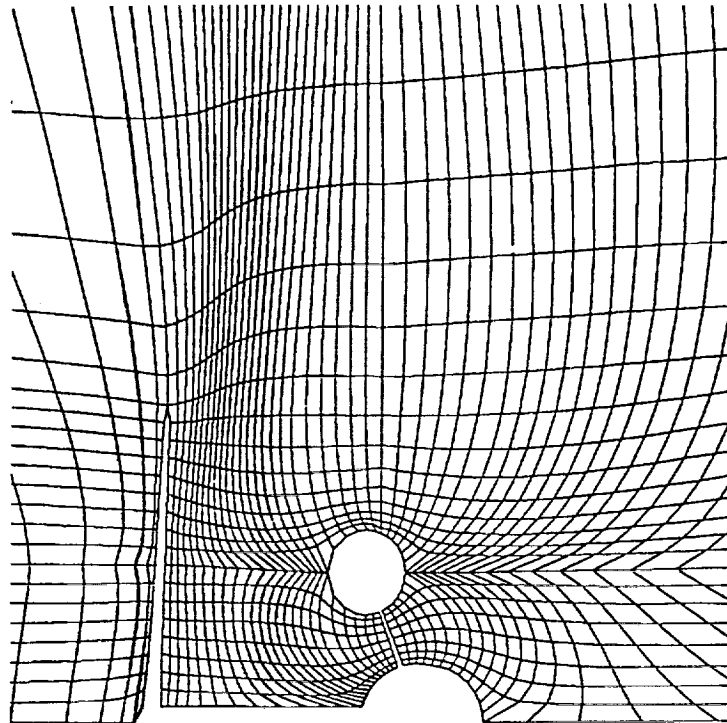


SIDE OF NACELLE

Fig. 5. Field Grids on Streamwise Cuts



WING/BODY INTERSECTION



AFTBODY SECTION

Fig. 6. Grids on the Wake

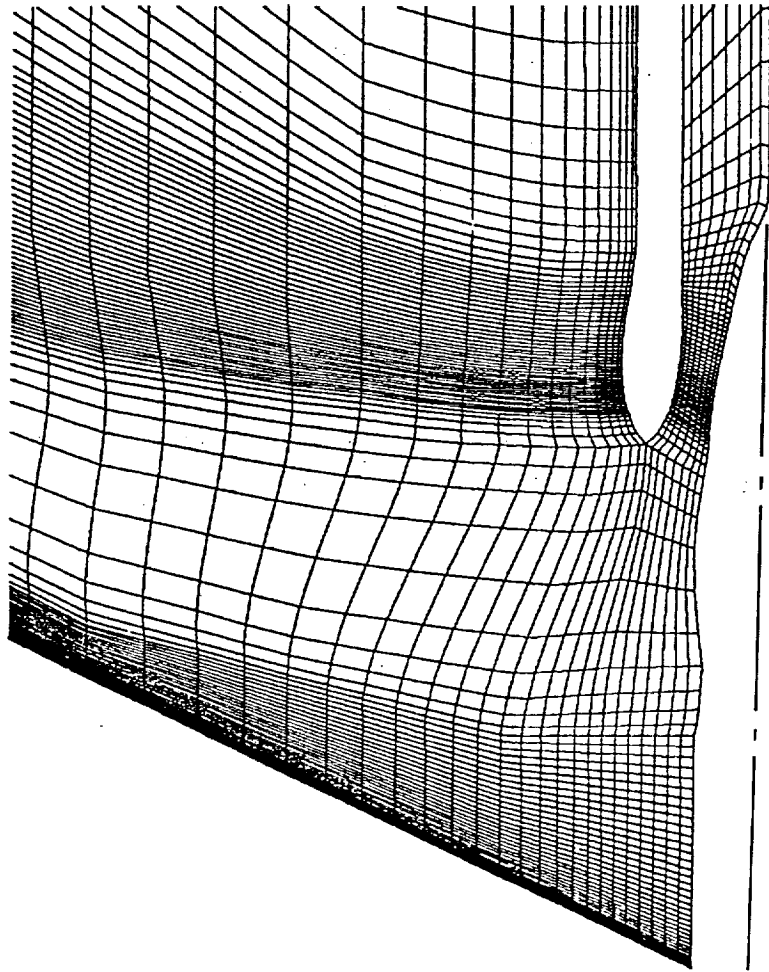


**Fig. 7. Surface Grids and Partial Field Grid for an
Aft-Mounted Propfan Airplane**

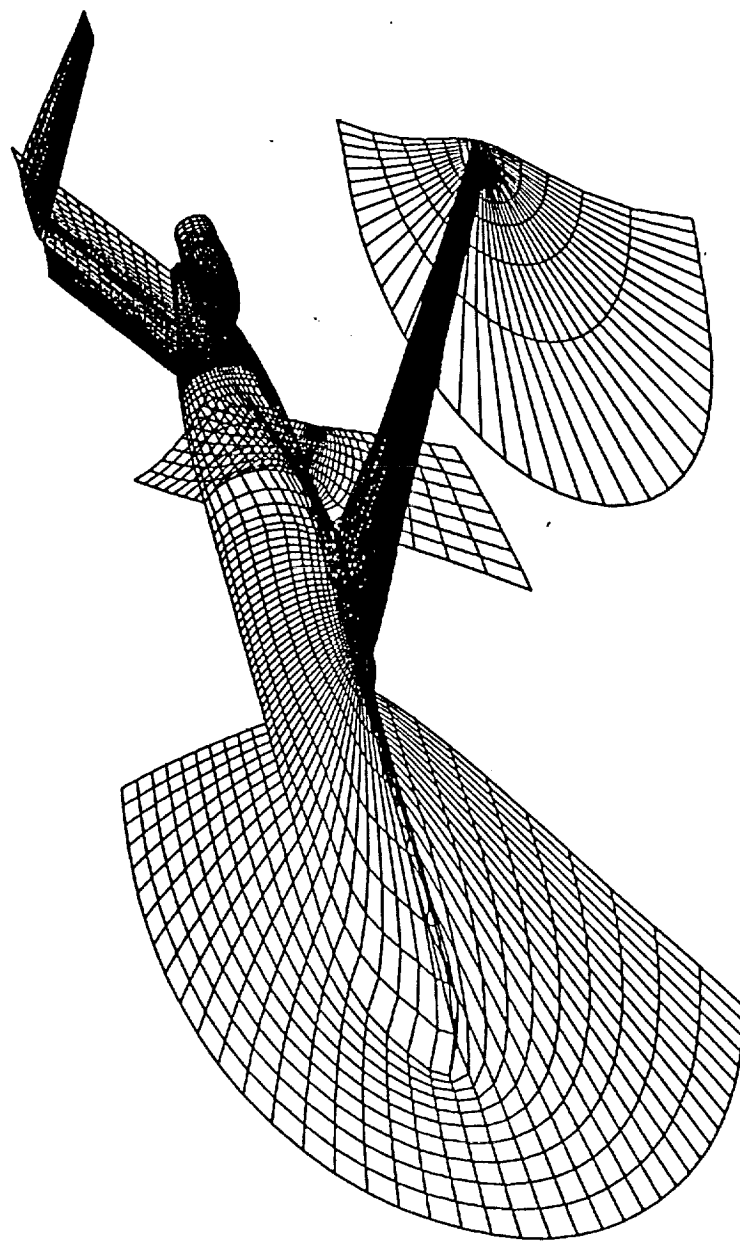


Fig.8. Convergence in Multigrid Cycles

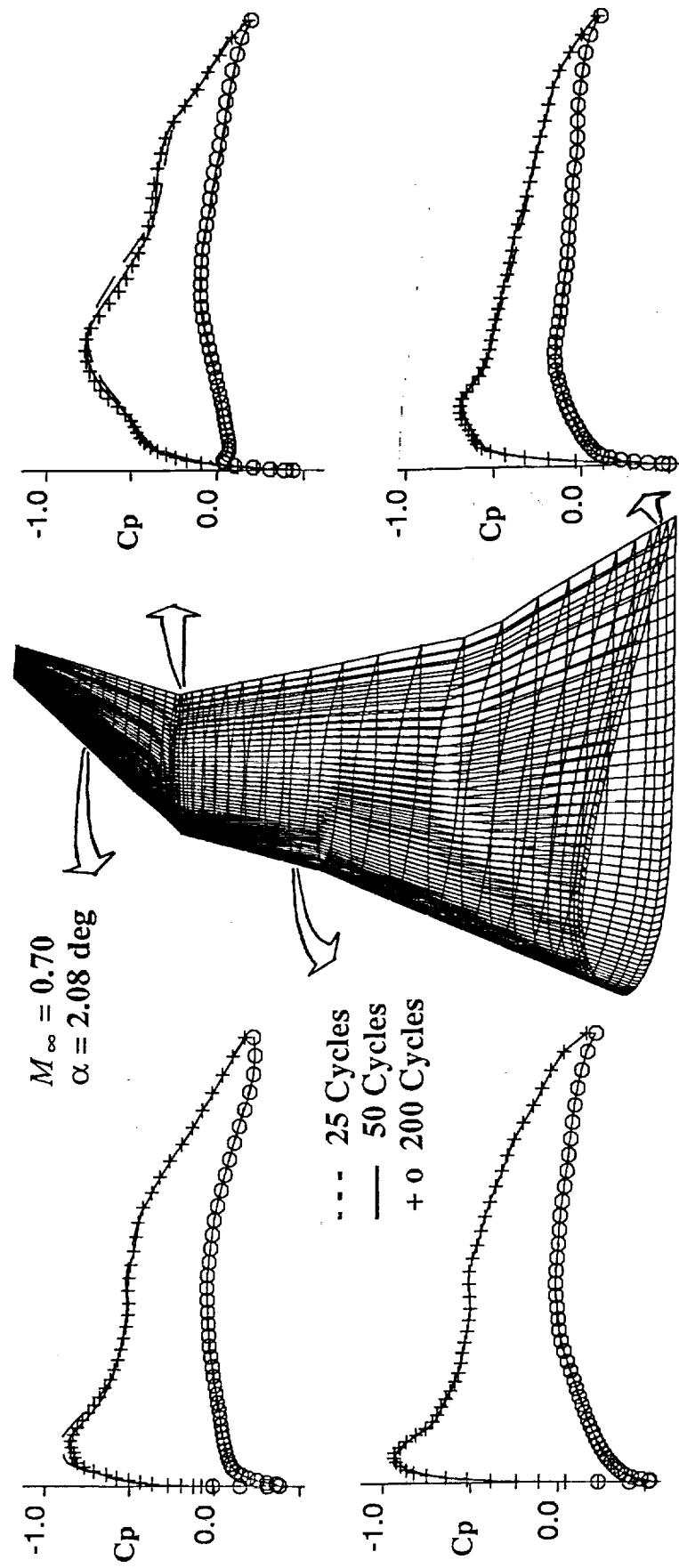


Fig. 9. Solution Sensitivity to Dissipation Parameters

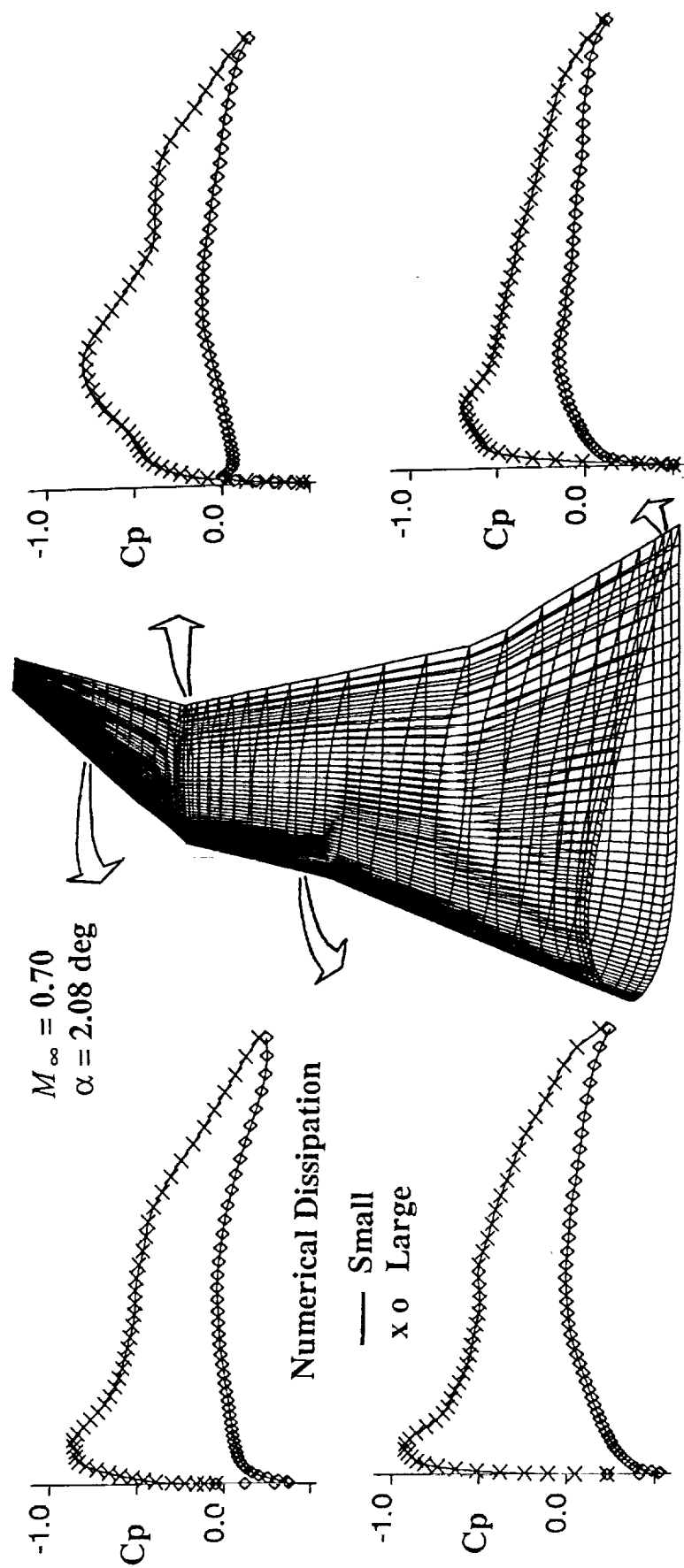


Fig. 10. Solution Sensitivity to Grid Quality

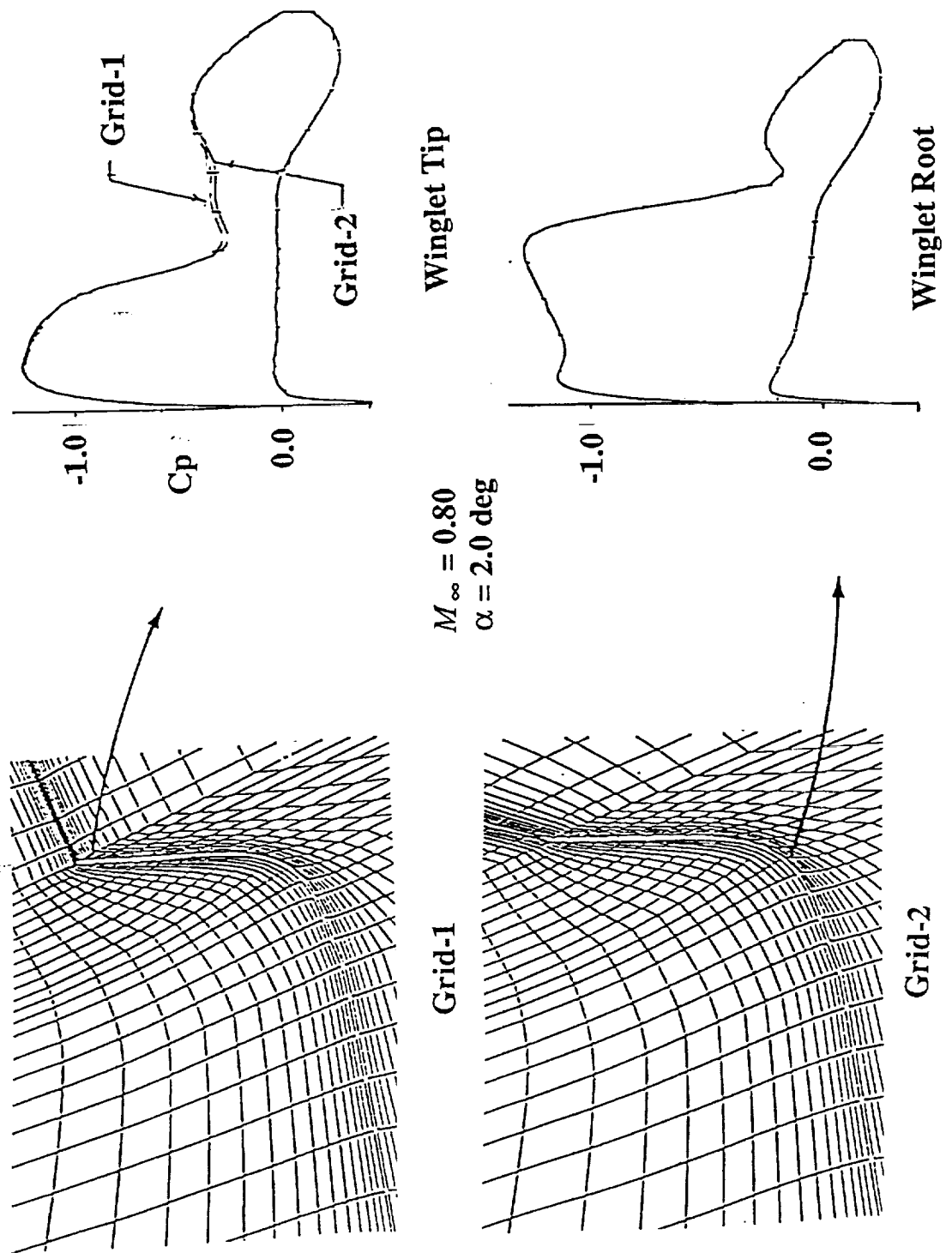


Fig. 11. Convergence in Mesh Refinement

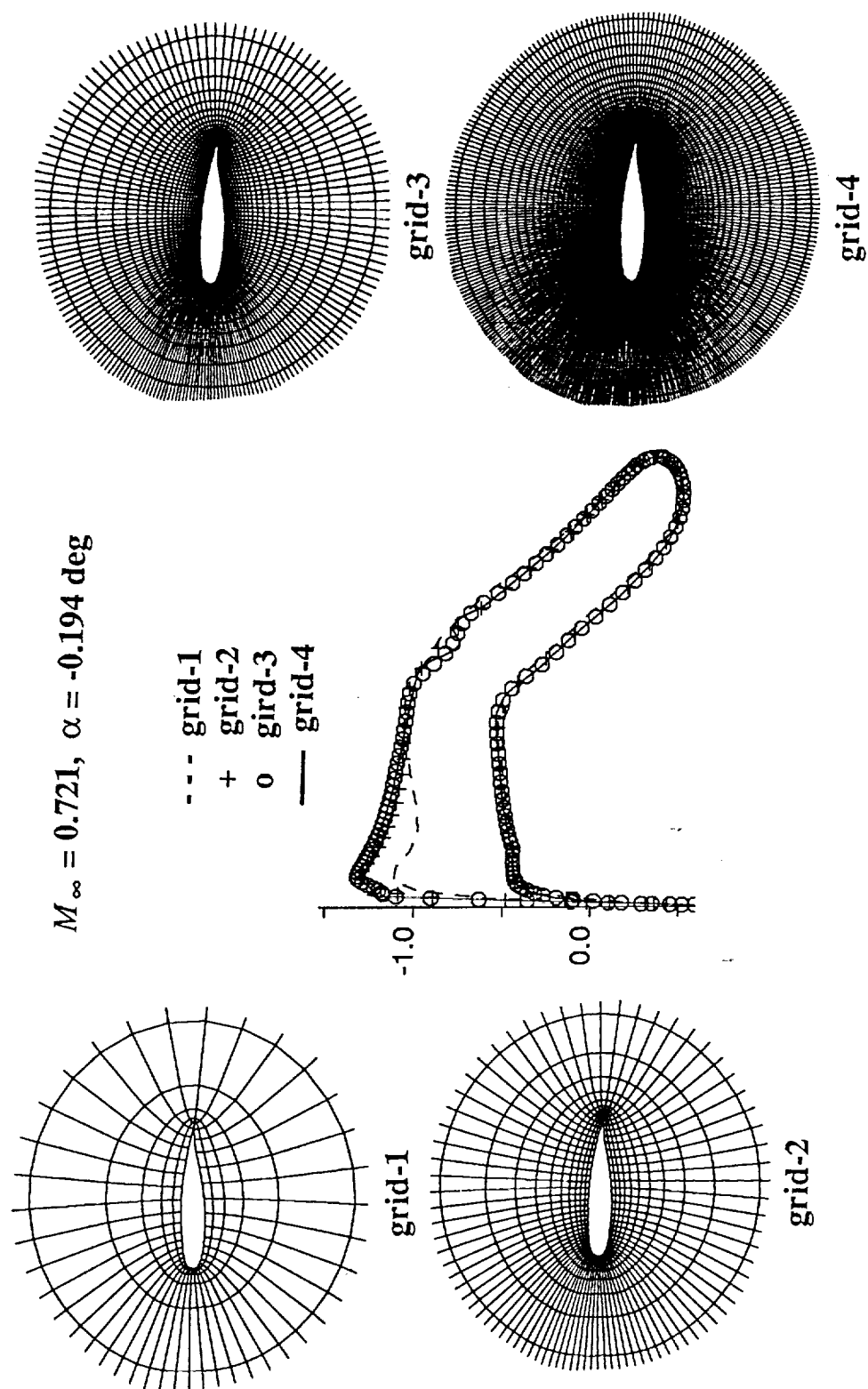


Fig. 12. Embedded Grid for a Domed Nacelle/Strut

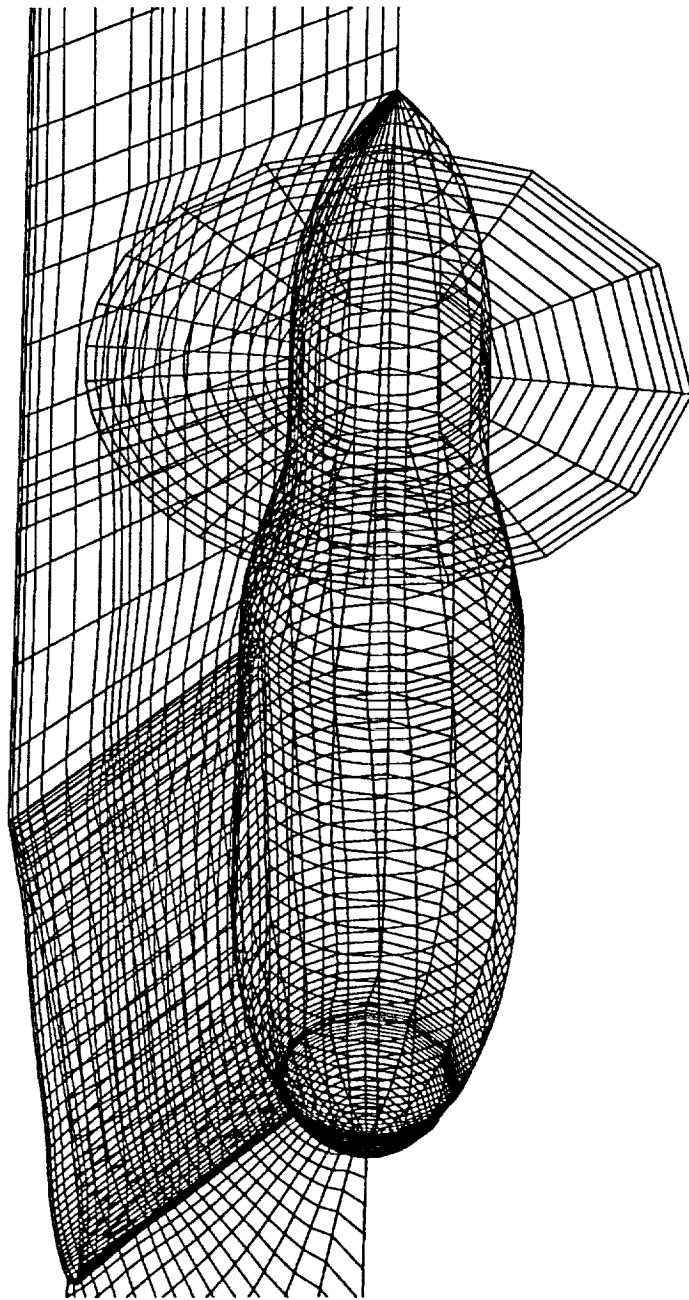


Fig. 13. C-Grid for Nacelle with Inlet and Exhaust

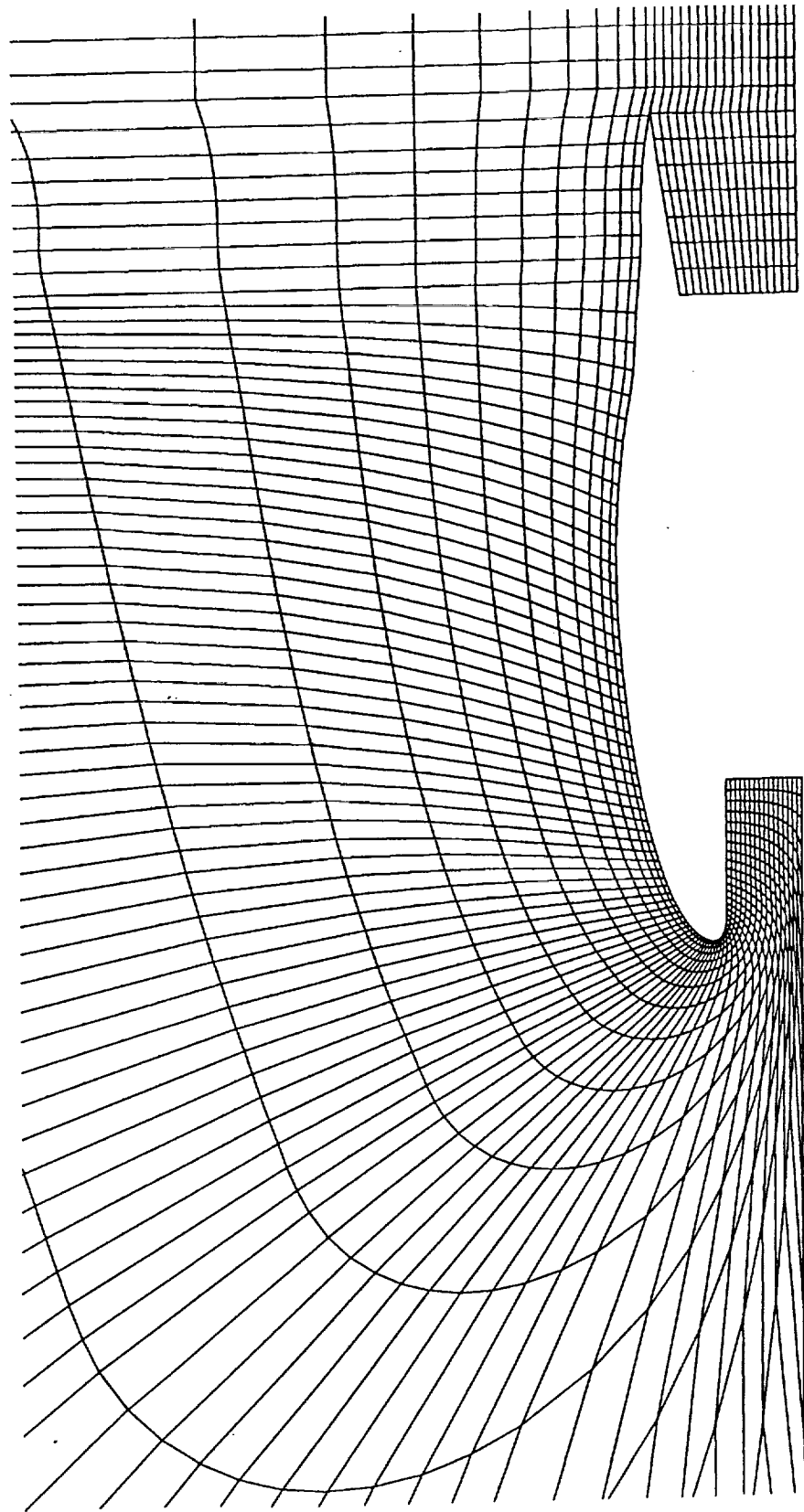


Fig. 14. Complete Flowfield Analysis

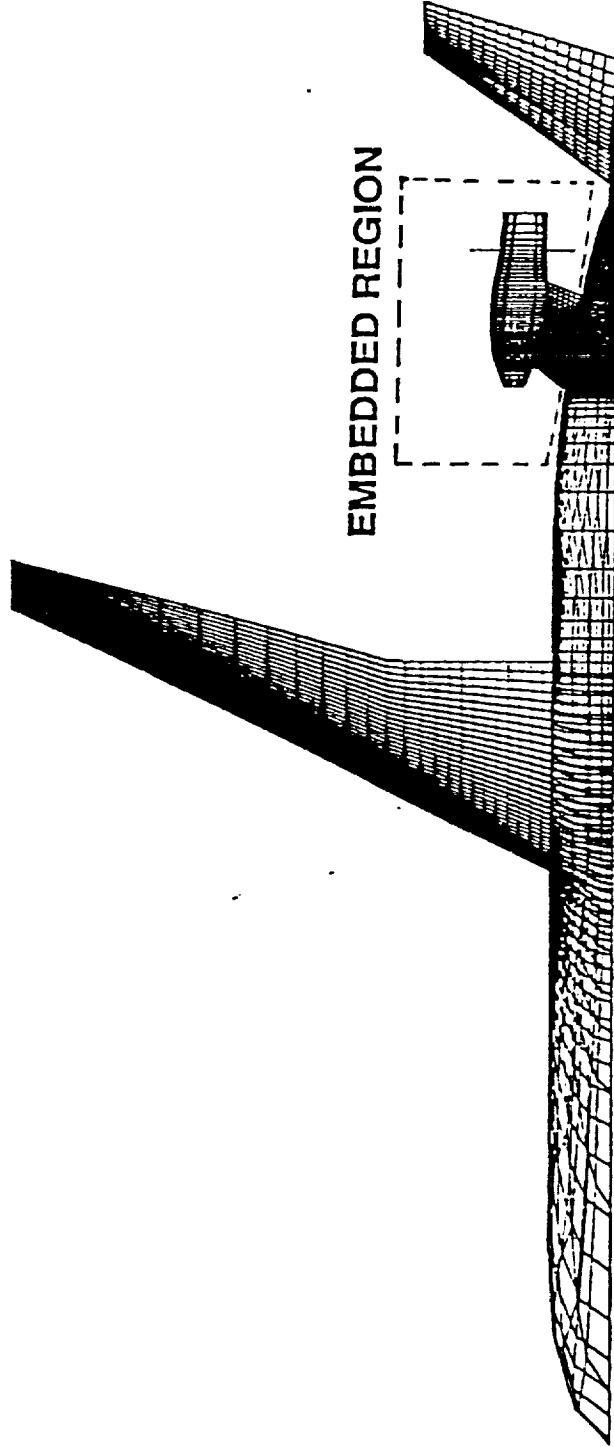
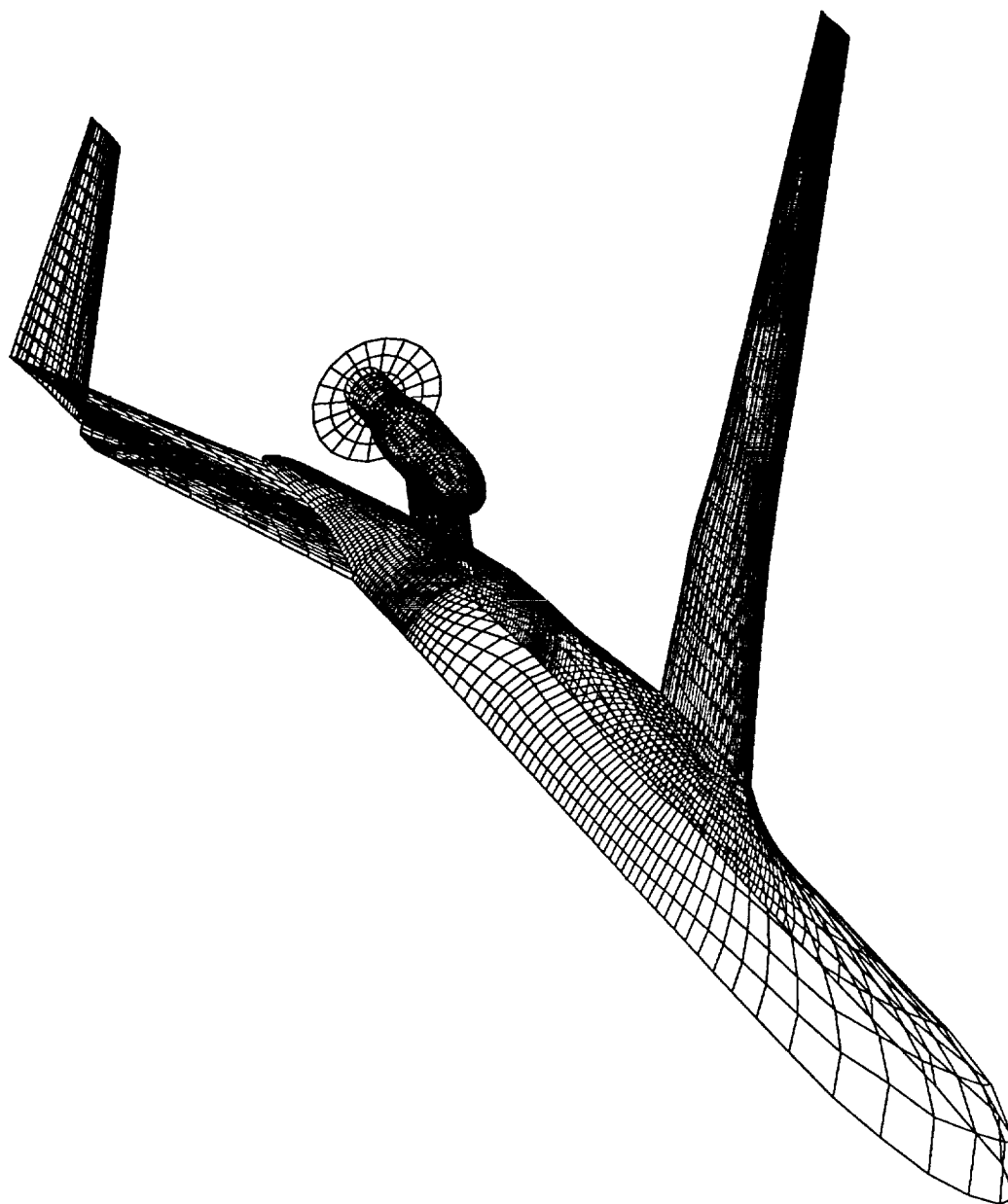


Fig. 15. Surface Grid for an Aft-mounted Propfan Aircraft



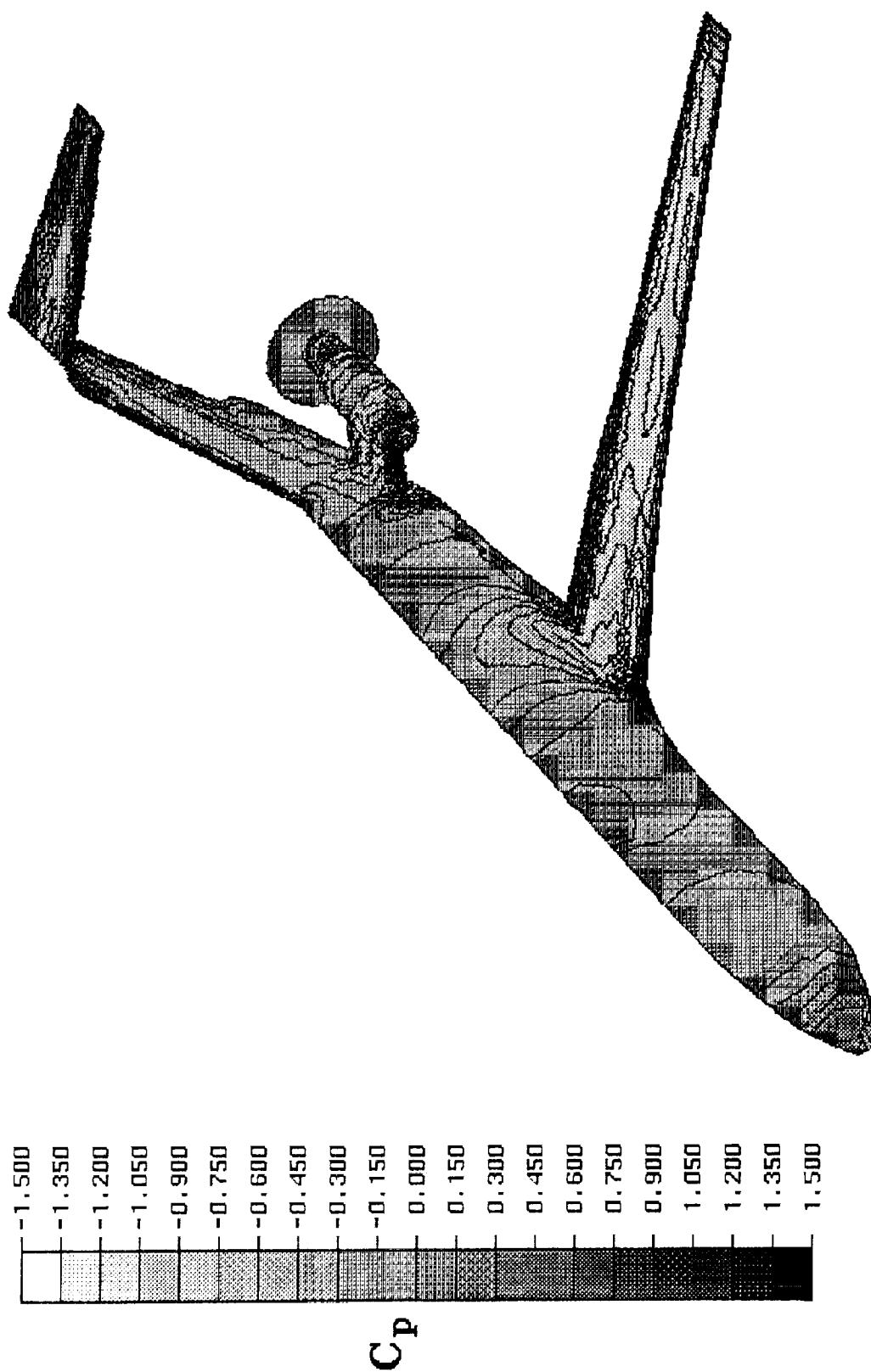
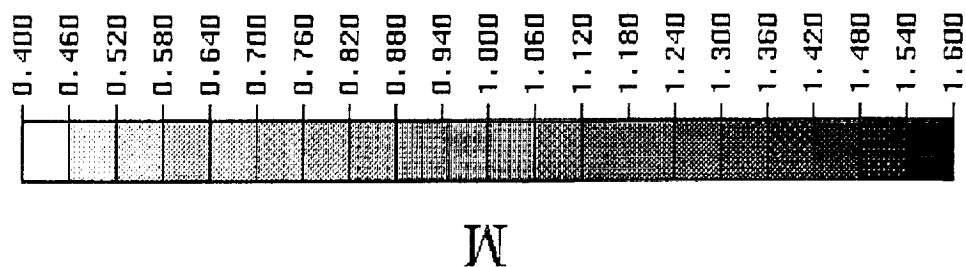
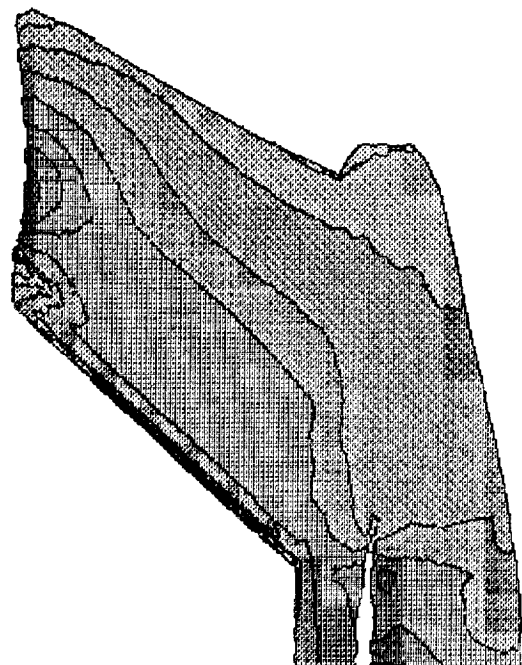


Fig. 16. Isobars for an Advanced Propfan Aircraft at Mach=0.8, Alpha=1.5



Propeller Off



Propeller On

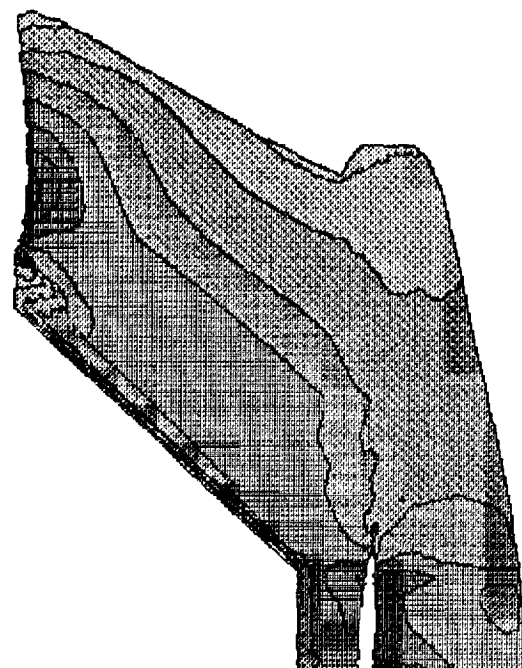


Fig. 17. Mach Contours on Fuselage Aftbody/Vertical Tail for an Advanced Propfan Configuration at Mach=0.8, Alpha=1.5

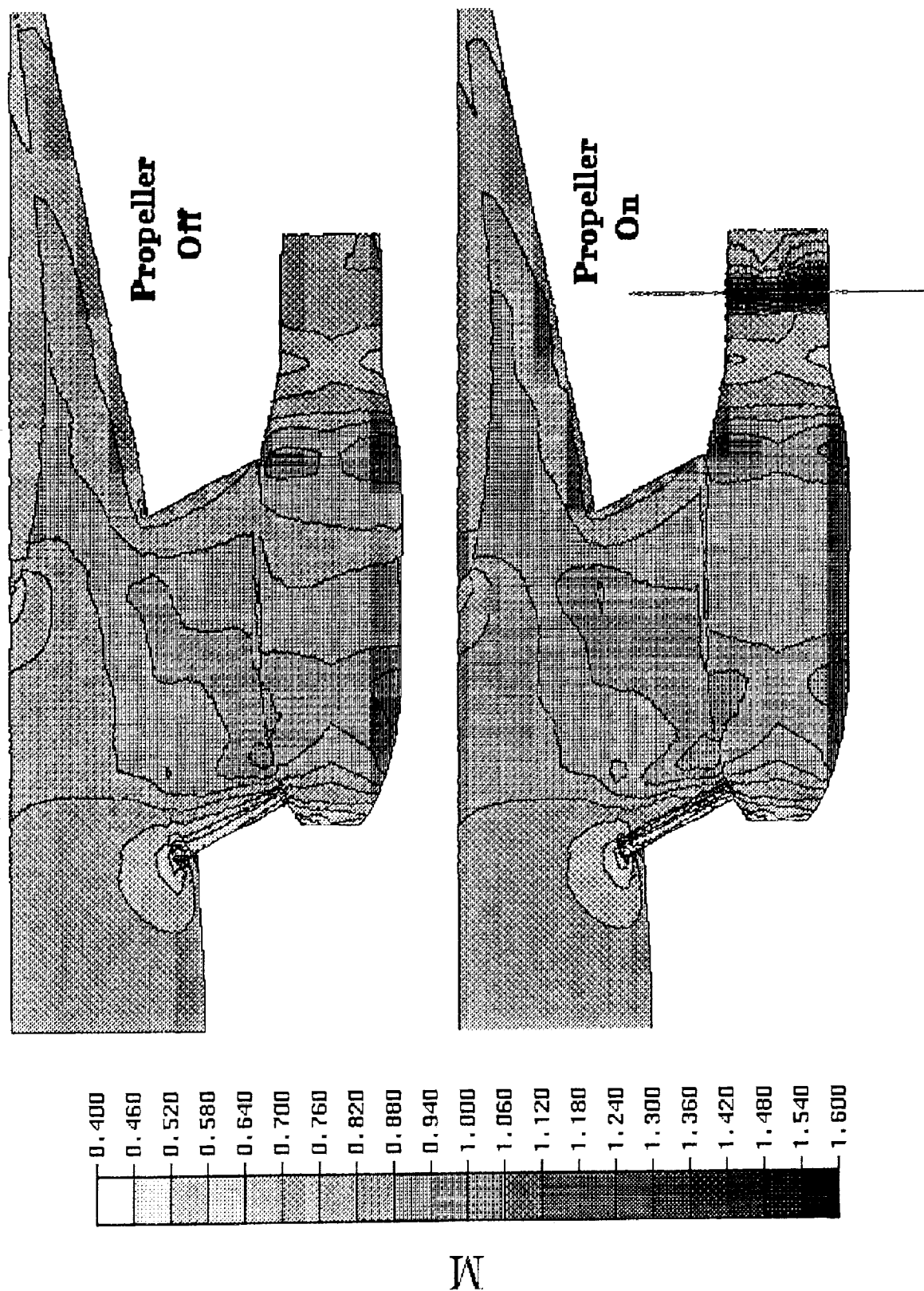
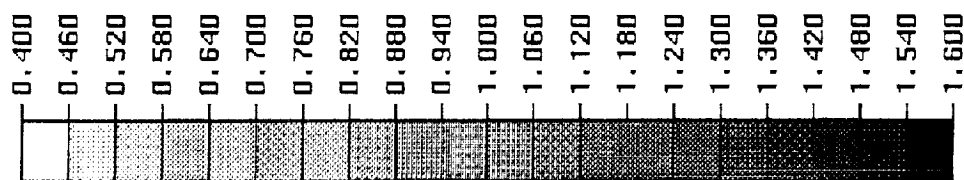


Fig. 18. Mach Contours in Aftbody Regions for an Advanced Propfan Configuration at Mach=0.8, Alpha=1.5, Upper Surface



M

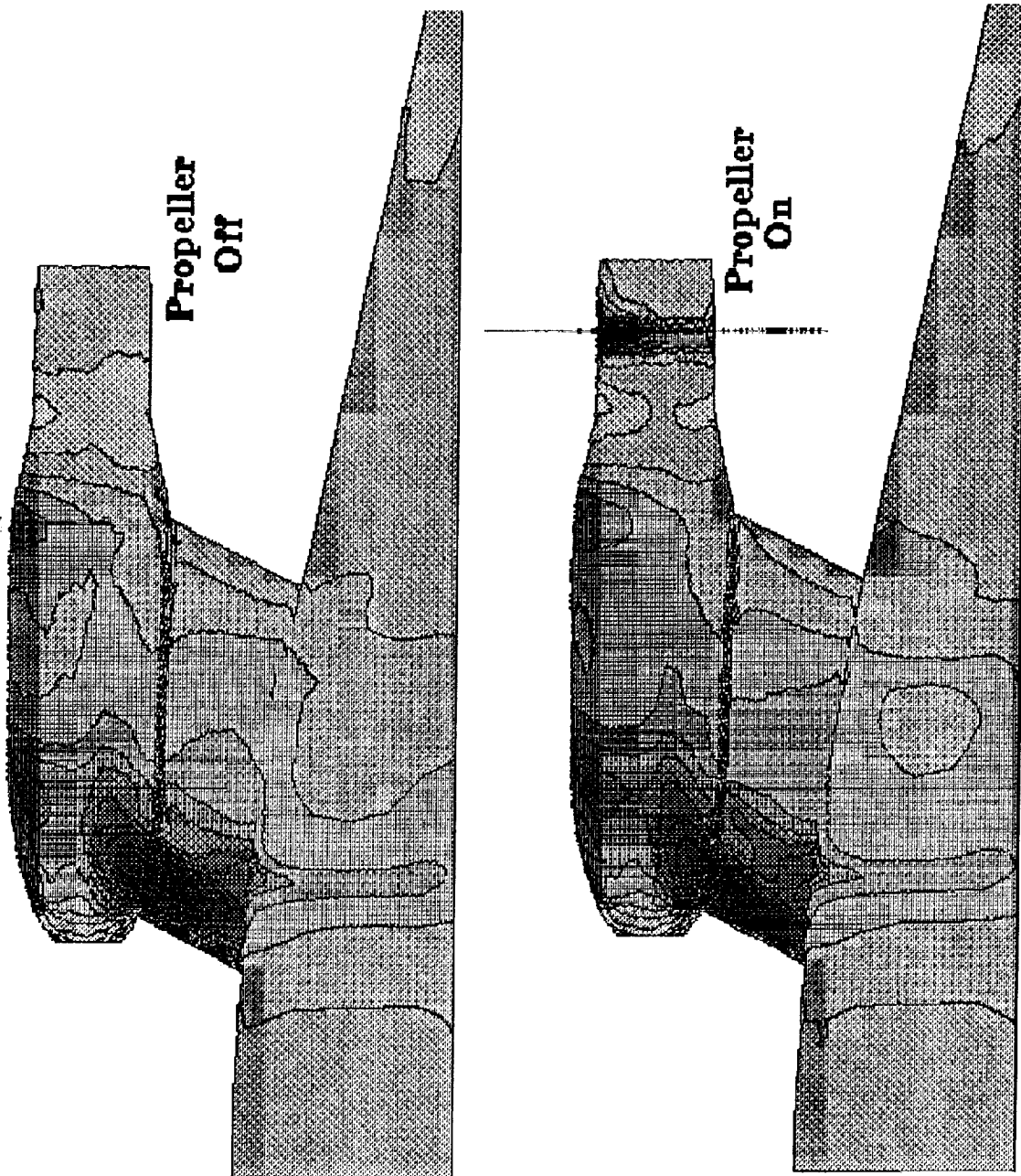
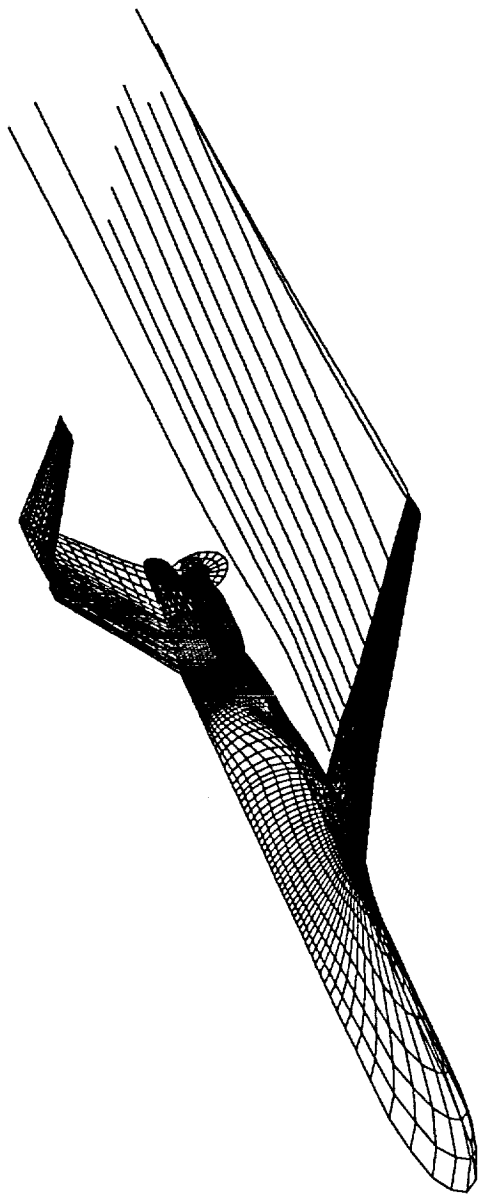


Fig. 19. Mach Contours in Aftbody Regions for an Advanced Propfan Configuration at Mach=0.8, Alpha=1.5, Lower Surface

Fig. 20. Streamline Tracing for an Aft-Mounted Propfan Aircraft



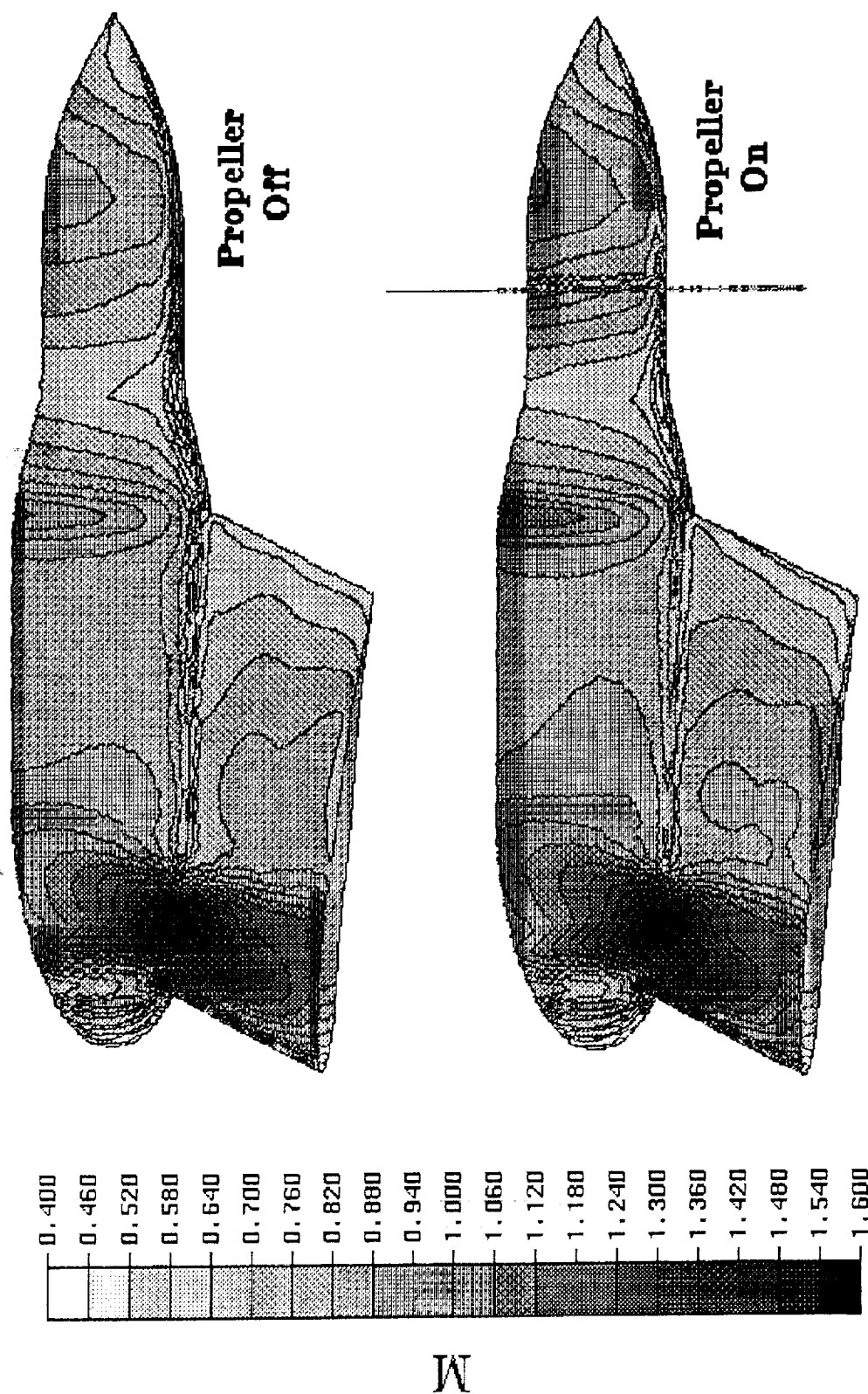


Fig. 21. Comparisons of Embedded Solutions in the Propfan Engine Regions, Mach=0.8, Alpha=1.5, Lower Surface

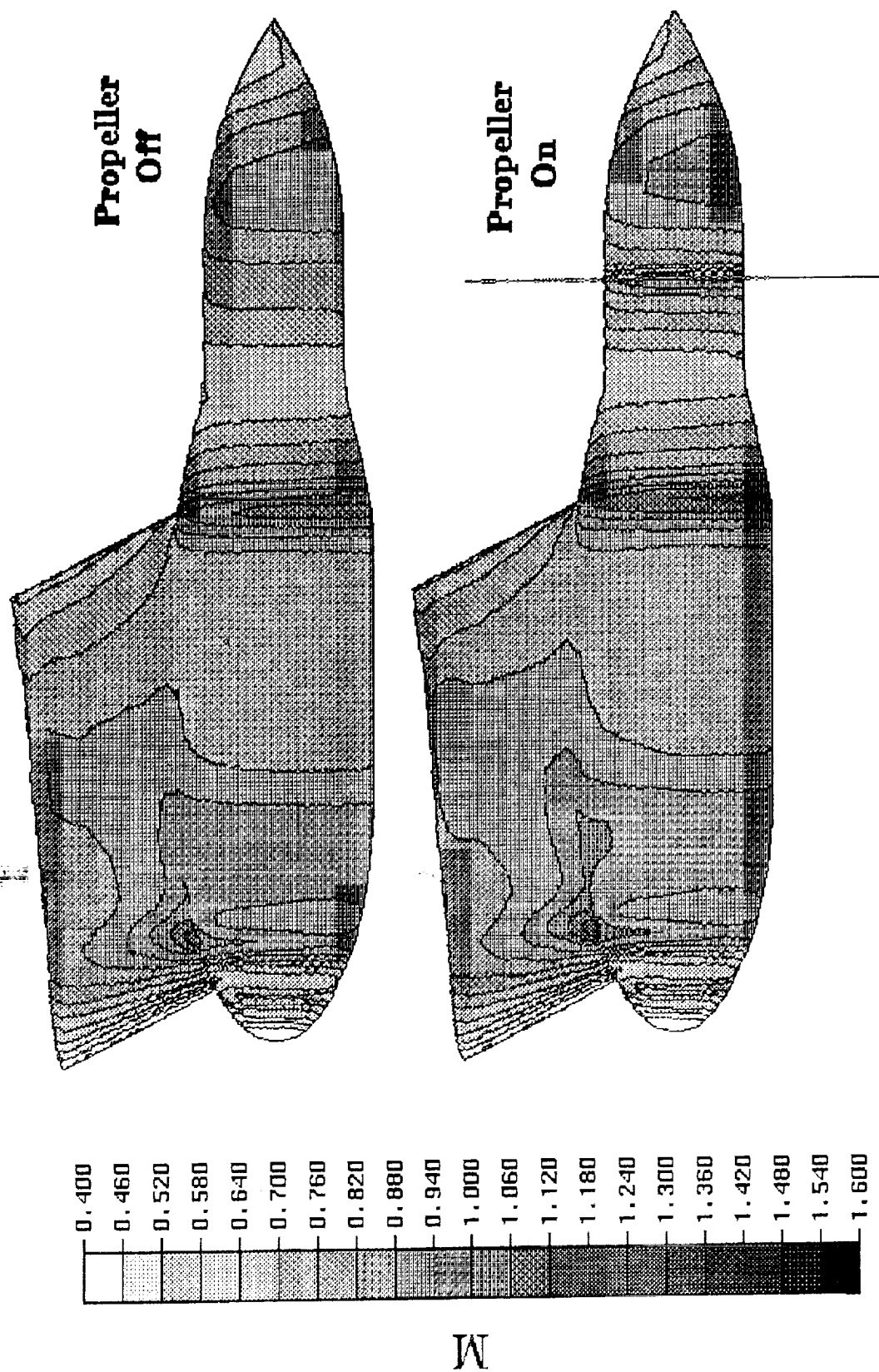
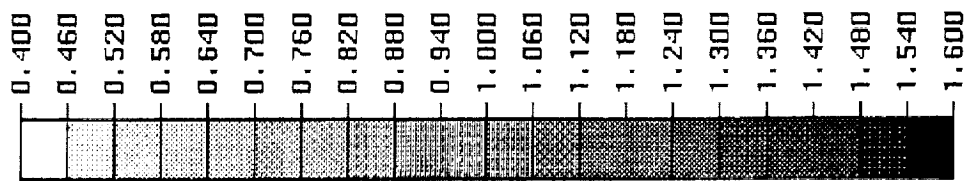
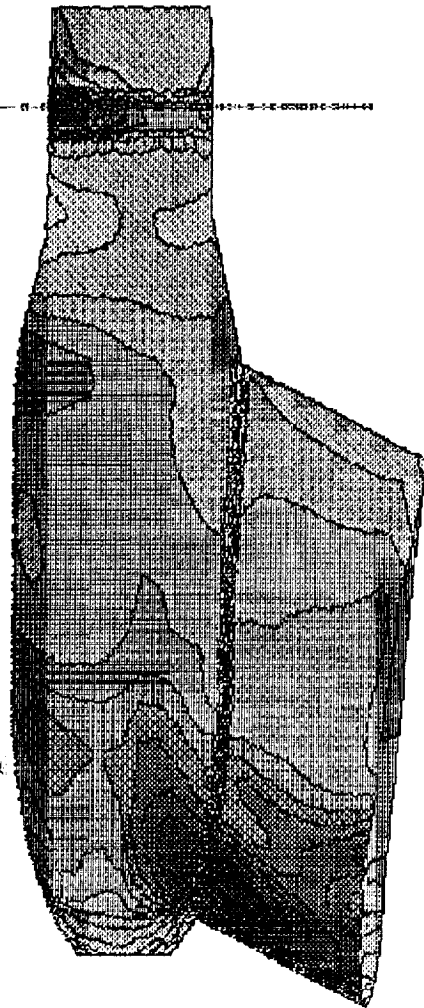


Fig. 22. Comparisons of Embedded Solutions in the Propfan Engine Regions, Mach=0.8, Alpha=1.5, Upper Surface



M

Global Solution



Embedded Solution

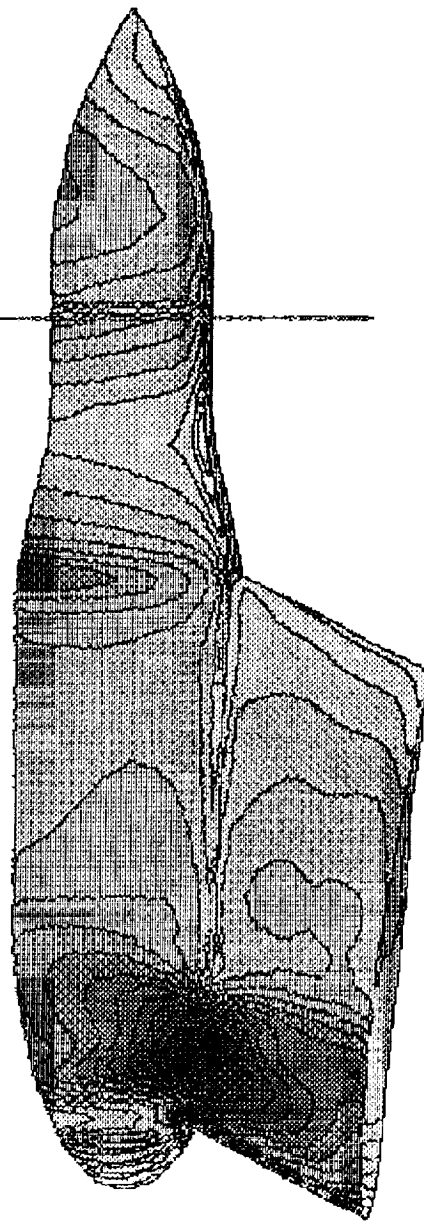


Fig. 23. Comparisons of Global/Embedded Solutions in the Propfan Engine Regions at Mach=0.8, Alpha=1.5, Lower Surface

1. Report No. NASA CR-181924, Volume I		2. Government Accession No.		3. Recipient's Catalog No.	
4. Title and Subtitle DEVELOPING AND UTILIZING AN EULER COMPUTATIONAL METHOD FOR PREDICTING THE AIRFRAME/PROPULSION EFFECTS FOR AN AFT-MOUNTED TURBOPROP TRANSPORT, VOLUME I: THEORY DOCUMENT				5. Report Date March 1991	
				6. Performing Organization Code	
7. Author(s) H. C. Chen and N. J. Yu				8. Performing Organization Report No.	
				10. Work Unit No.	
9. Performing Organization Name and Address Boeing Commercial Airplane Group P.O. Box 3707 Seattle, Wa. 98124-2207				11. Contract or Grant No. NAS1-18703	
				13. Type of Report and Period Covered Contractor Report	
12. Sponsoring Agency Name and Address National Aeronautics and Space Administration Langley Research Center Hampton, VA 23665-5225				14. Sponsoring Agency Code 535-03-10-01	
15. Supplementary Notes Langley Technical Monitor: William P. Henderson Final Report					
16. Abstract <p>An Euler flow solver has been developed for predicting the airframe/propulsion integration effects for an aft-mounted turboprop transport. This solver employs a highly efficient multigrid scheme, with a successive mesh-refinement procedure to accelerate the convergence of the solution. A new dissipation model has also been implemented to render solutions that are grid insensitive. The propeller power effects are simulated by the actuator disk concept. An embedded flow-solution method has been developed for predicting the detailed flow characteristics in the local vicinity of an aft-mounted propfan engine in the presence of a flowfield induced by a complete aircraft. Results from test case analysis are presented. A user's guide for execution of computer programs, including format of various input files, sample job decks, and sample input files, is provided in an accompanying volume.</p>					
17. Key Words (Suggested by Author(s)) Euler Method, Airframe/Propulsion Effects, Aft-Mounted Turboprop			18. Distribution Statement Unclassified - Unlimited Subject Category 02		
19. Security Classif. (of this report) Unclassified		20. Security Classif. (of this page) Unclassified		21. No. of pages 50	
				22. Price	